High-Resolution Modeling and Prediction of Urban Floods Using WRF-Hydro and Data Assimilation

by

Sunghee Kim[1,&], Haojing Shen[1,*], Seongjin Noh[1,#], Dong-Jun Seo[1], Edwin Welles[2], Erik Pelgrim[3], Albrecht Weerts[3,4], Eric Lyons[5], Brenda Philips[6]

[1]Dept of Civil Eng, The University of Texas at Arlington, Arlington, TX 76019
[2]Deltares USA, Silver Spring, MD 20910
[3]Deltares, Delft, The Netherlands
[5]Engineering Computer Services, Univ of Massachusetts Amherst, MA 01003
[6]Dept of Electrical and Computer Eng, Univ of Massachusetts Amherst, Amherst, MA 01003

Submitted to the Journal of Hydrology

Aug 1, 2020

---

[*]Corresponding author, e-mail address: haojing.shen@mavs.uta.edu
[&]Now at Lynker Technologies, Leesburg, VA
[#]Now at Kumoh National Institute of Technology, Gumi, The Republic of Korea
[4]Hydrology and Quantitative Water Management Group, Wageningen University, Wageningen, The Netherlands

Abstract

We assess the impact of increasing the resolution of hydrologic modeling, calibration of selected model parameters and assimilation of streamflow observation toward event-based urban flood modeling and prediction using WRF-Hydro in the Dallas-Fort Worth area (DFW). We use quantitative precipitation estimates at 500-m 1-min resolution from the Collaborative Adaptive Sensing of the Atmosphere radar network for observed rainfall, Stepwise Line Search for calibration, and fixed-lag smoothing for data assimilation (DA). The model domain is a 144.6 km^2 area comprising 3 urban catchments in Arlington and Grand Prairie in the middle of DFW. It is shown that event-specific calibration of 6 WRF-Hydro parameters is largely successful in simulating hydrographs at the catchment outlets particularly for the most important rising limbs, but less so for attenuated peaks or fast-receding falling limbs. A spatial resolution of at least 250 m was necessary for the land surface model (LSM) to delineate small catchments and hence to capture catchment-wide rainfall with acceptable accuracy. Simulations at selected combinations of resolutions, 250 and 125 m for the LSM and 250, 125, 50 m for the routing models, showed mixed results. The overall results indicate that, in the absence of resolution-specific prescription and calibration of channel routing parameters, a resolution of 250 m for both the LSM and routing models is a good choice in terms of performance and computational requirements, and that, in the absence of high-quality calibration and continuous simulation of streamflow, DA is necessary to initialize WRF-Hydro for event-based high-resolution urban flood prediction.
Key words: urban flood, high resolution, precipitation, hydrologic modeling, prediction, data assimilation

1 Introduction

With the implementation of the National Water Model (NWM), the National Weather Service (NWS) has made a step-change advance in operational water forecasting by enabling high-resolution (1 hr, 1 km for land surface and 250 m for routing) hydrologic modeling across the US (NWS 2020). As a part of the NWM initiative, the NWS has been mandated to provide forecasts at even higher spatiotemporal resolutions when and where such information is demanded such as in large urban areas for flood warning, and areas of high-value infrastructure, susceptible to landslides, or impacted by forest fires (Graziano et al. 2017). The value of high-resolution products and services depends not only on the hydrologic and hydraulic models but also on the quality of the forcings, model parameters, initial conditions (IC) and boundary conditions at the commensurate resolutions. In the DFW area, the Collaborative Adaptive Sensing of the Atmosphere (CASA) Program operates a network of X-band radars to provide a suite of meteorological, hydrometeorological and hydrologic products for severe weather and flash flood monitoring and prediction (Chandrasekar et al. 2013). The network currently consists of 7 radars located at Addison, Arlington, Cleburne, Denton, Fort Worth, Mesquite and Midlothian, TX. A salient feature of the above operation is that the radar rainfall data are available at a very high resolution of 500 m and 1 min. The CASA quantitative precipitation estimates (QPE) are currently input to the NWS Hydrology Laboratory-Research Distributed Hydrologic Model (HL-RDHM, Koren et al. 2004, NWS 2009) to produce a suite of hydrologic products at the same resolution in real time (Rafieeinasab et al. 2015, Habibi et al. 2016, Habibi and Seo 2018). The characteristic spatial scale of natural and man-made physiographic features in the study area suggests that a further increase in hydrologic model resolution may improve the information content of the model output (Habibi et al. 2019). There is also an ever increasing demand for higher resolution hydrologic products for enhanced spatio-temporal specificity. The purpose of this work is to assess using WRF-Hydro how increasing the resolution of hydrologic modeling, calibration of selected model parameters and assimilating locally-available observations of precipitation and streamflow may improve flood modeling and prediction toward high-resolution water forecasting in urban areas.

Real-time continuous operation of high-resolution models is computationally very expensive particularly for large areas (Habibi et al. 2019). A more practical approach is likely to be event-based operation with robust initialization. As such, our assessment is carried out in the context of event-based modeling and prediction. The event-based paradigm meant that most conventional calibration methods, which rely on time-continuous observations of precipitation and streamflow, and sequential DA methods, which employ recursive state updating, may not be applicable or desirable. To that end, we employ multi-event averaging of event-specific parameter optimization results for calibration and reduced-rank fixed-lag smoothing for DA. The new contributions of this paper are: selective calibration of WRF-Hydro for urban flood modeling and prediction, improving simulation of highly peaked hydrographs with the addition of a conditional bias (CB) penalty, and assessment of the impacts of different spatio-temporal resolutions of rainfall-runoff and routing models, of ICs and land cover, and of assimilation of streamflow observations for initialization of WRF-Hydro toward event-based operation of high-resolution urban flood prediction. This paper is organized as follows. In Section 2, we describe the study area, data used and the hydrologic models used. Section 3 describes the methods used in the experiment design, calibration and DA. Section 4 describes the experiments and presents the results. Section 5 provides the conclusions and future research recommendations.

2 Study area, data and hydrologic models used

Here we describe the study area, data used and hydrologic models used.

2.1 Study area

The study area comprises the Johnson (40.2 km^2), Cottonwood (32.3 km^2) and Fish (54.6 km^2) Creek Catchments in the Cities of Arlington and Grand Prairie in the Dallas-Fort Worth (DFW) area of TX (see Fig 1a,b). These basins have been used in previous studies of high-resolution hydrologic modeling and sensing (Rafieeinasab et al. 2015, Norouzi 2016, Habibi et al. 2016, 2019). The Johnson, Cottonwood and Fish Creek Catchments, referred to herein as JC, CC and FC, respectively, are highly urbanized with impervious fractions of 0.48, 0.37 and 0.31, respectively (Habibi et al. 2019, see Fig 1a). Hydroclimatologically, the study basins are particularly challenging for hydrologic modeling and prediction due to very short memory in the surface and soil water storages. Recent assessment of the streamflow prediction skill of the NWS operational hydrologic models indicates that the study region has the smallest predictability among the 138 basins assessed in 8 different River Forecast Centers' (RFC) service areas across large sections of the US (Alizadeh et al. 2019).

2.2 Data used

The CASA QPE products have been extensively evaluated (Chandrasekar et al. 2012, Chen et al. 2016, Cifelli et al. 2018). Comparative evaluation of different radar-based QPE products (Rafieeinasab et al. 2014, 2015) showed that the CASA QPE is generally more accurate for larger precipitation amounts in the study area whereas the Multisensor Precipitation Estimator (MPE, Seo et al. 2010) estimates do better for smaller amounts. The CASA QPE operation recently began fusing the QPE from the X-band radar network with that from the WSR-88D in Burleson, TX (Chen and Chandrasekar, 2015). The rainfall estimates used in this study are the resulting fused QPE product. For details, the reader is referred to Chandrasekar (2017).

Because the CASA network has been in continuous operation only for several years, a long period of time-continuous data is not available. In this study, we used the 5 recent events of varying magnitude listed in Table 1. Fig 2 shows the total rainfall maps for the 4 largest events. All other forcings for WRF-Hydro are from the near real-time North American Land Data Assimilation System (NLDAS) Phase 2 forcing and model output produced operationally at the Environmental Modeling Center of the NOAA/NWS/National Centers for Environmental Prediction (Cosgrove et al. 2003). Networks of ALERT sensors operated by the Cities of Arlington and Grand Prairie provide water level observations in the study area including at the catchment outlets. The observations are based on pressure transducers located at the channel bottom. To estimate discharge from stage observations, we used rating curves derived by Norouzi (2016) at the outlets of the 3 catchments (see Fig 1a) based on the numerical modeling approach of Kean and Smith (2004, 2005, 2010).

2.3 Hydrologic model used

The hydrologic model used is WRF-Hydro Version 5.0.2. (Gochis et al. 2018). For urban flood modelling, the most important components are the rainfall-runoff, terrain, or hillslope, routing and channel routing models. Below, we describe only the core model dynamics that are directly relevant to the development of this work.

2.4 Rainfall-runoff model

The rainfall-runoff option used in this work is the Simple Water Balance model (SWB) of Schaake et al. (1996) which is used by the NWM also. As in Moore (1985) and the SCS curve number method (USDA 1986), the SWB models the average runoff depth over a grid box or a catchment, Q_s, as (Schaake et al. 1996):

$$Q_s = \frac{P_x^2}{(P_x + I_c)^2} \quad (1)$$

where P_x and I_c denote the average precipitation depth and infiltration capacity over the grid box. The infiltration capacity, I_c, in Eq. (1) is modeled as (Schaake et al. 1996):

$$I_c = D_x(1 - e^{-kt}) \quad (2)$$

Where D_x denotes the maximum water holding capacity of the soil column, k denotes the decay coefficient and t denotes the time elapsed. Eq. (2) is analogous to the potential infiltration depth, F, of the Horton infiltration model (Horton 1940) without the constant infiltration rate due to gravity:

$$F = \frac{f_o}{k}(1 - e^{-kt}) \quad (3)$$

where f_0 denotes the initial potential infiltration rate due to suction pressure and k denotes the decay rate. One may hence interpret the maximum soil water holding capacity, D_x, as representing f_0/k in Eq. (2) where $1/k$ represents the time scale of decay of potential infiltration rate. The maximum water holding capacity D_x in Eq. (2) is modeled as (Schaake et al. 1996):

$$D_x = \sum_{i=1}^{4} \Delta Z_i(\theta_{sat} - \theta_i) \quad (4)$$

where ΔZ_i denotes the thickness of the i-th soil layer, θ_{sat} denotes the saturation soil water content (i.e., porosity) and θ_i denotes the initial soil water content in the i-th soil layer. Eq. (4) is analogous to the total infiltration depth in the Green-Ampt infiltration equation (Green and Ampt 1911):

$$F = Z_f(\theta_{sat} - \theta_{init}) \quad (5)$$

where Z_f denotes the depth to the wetting front and θ_{init} denotes the vertically uniform initial soil water content. As shown above, the surface runoff component of the SWB may be considered as a combination of the SCS method for runoff ratio and the Horton infiltration equation without the gravity term for time decay in potential infiltration rate in which the maximum water holding capacity is prescribed by the depth-integrated soil pore space given the antecedent soil water content. The study area is highly urbanized. Accurate high-resolution depiction of land cover is hence very important (Rafieeinasab et al. 2015, Norouzi 2016, Habibi et al. 2016). WRF-Hydro uses the United States Geological Survey's (USGS) 24-category land cover product (Loveland et al. 1995, see Fig 1c) to parameterize the Land Surface Model (LSM). In this work, we use the USGS's National Land Cover Database (Wickham et al. 2019) for higher resolution depiction (see Fig 1d) and compare with the USGS 24-category land cover.

2.5 Terrain routing model

The terrain, or hillslope, routing option used in this work is the diffusive wave model. The mass balance equation is given by:

$$\frac{\partial h}{\partial t} + \frac{\partial q_x}{\partial x} + \frac{\partial q_y}{\partial y} = i_e \quad (6)$$

where h denotes the water depth, q_x and q_y denote the specific discharge along the x- and y-directions, respectively, and i_e denotes the excess precipitation, or surface runoff depth, given by the rainfall-runoff model. Though expressed as a 2D model, Eq. (6) is solved only along the steepest-descending direction, referred to as the D8 option in WRF-Hydro (Gochis et al. 2018). The momentum balance equation is given by:

$$-\frac{\partial h}{\partial x} + S_{ox} = S_{fx} = \left(\frac{n_{ov} q_x}{h^{5/3}}\right)^2 \tag{7}$$

where S_{ox} denotes the terrain or channel bed slope, S_{fx} denotes the friction slope and n_{ov} denotes the Manning's friction coefficient for the hillslope. The last equality in Eq. (7) follows from the Manning's equation under the wide channel assumption (Akan and Houghtalen 2013). In WRF-Hydro, S_{ox} is calculated based on the DEM data and n_{ov} is prescribed according to land cover. As such, the choice of the land cover data impacts terrain routing.

2.6 Channel routing model

The channel routing option used in this work is the gridded diffusive wave model which solves the following mass and momentum balance equations:

$$\frac{\partial A}{\partial t} + \frac{\partial Q}{\partial x} = q_l \tag{8}$$

$$-\frac{\partial h}{\partial x} + S_o = S_f = \left(\frac{nQ}{AR^{2/3}}\right)^2 \tag{9}$$

where A denotes the wetted channel cross-sectional area, Q denotes the flow rate, q_l denotes the lateral inflow from Eqs. (6) and (7), h denotes the water depth, S_o denotes the channel bed slope, n denotes the Manning's roughness coefficient for the channel bed and R denotes the hydraulic radius of the channel cross section. The resulting finite difference equation is solved iteratively using the Newton-Raphson method (Gochis et al. 2018). The channels are delineated based on the National Hydrographic Dataset Plus Version 2 (NHDPlusV2, Moore et al. 2019). The channel routing model assumes trapezoidal cross section for which two additional parameters, the channel bottom width and side slope, are necessary:

$$Q = \frac{1}{n} A R^{2/3} {S_f}^{1/2} = \frac{1}{n} \frac{\left((B_w + zh)h\right)^{5/3}}{\left(B_w + 2h\sqrt{1+z^2}\right)^{2/3}} {S_f}^{1/2} \tag{10}$$

where B_w denotes the channel bottom width, z denotes the channel side slope and h denotes the water depth. WRF-Hydro prescribes the above parameters stream order-specifically, i.e., channels of the same Strahler stream order share the same parameter values for channel routing (Gochis et al. 2018).

3 Methods

To assess how the resolution of hydrologic modeling, calibration, and DA may impact urban flood modeling and prediction using WRF-Hydro, we designed and carried out a set of simulation experiments. In this section, we describe the experiment design, calibration and DA.

3.1 Design of experiments

Table 2 shows the combinations of resolutions considered in this work. The CASA QPE is available at 500 m 1 min resolution. Rafieeinasab et al. (2015) report that a resolution of 500 m and 15 min or higher is necessary for streamflow prediction at the outlets of the study basins using CASA QPE and HL-RDHM (Koren et al. 2004). To assess how higher spatial resolution of hydrologic modeling may improve flood simulation in the study area, we disaggregate the 500 m QPE to QPEs at nominal resolutions of 250 m and 125 m by remapping the CASA QPE on a lat-lon grid to a Lambert conformal conic grid for ingest by WRF-Hydro. For the remapping, we used the conserve method available for ESMF (NCAR 2020). In addition, to assess possible gains from higher temporal resolution modeling, we aggregated the native resolution 1 min CASA QPE to 10 min accumulations. With the above choices, the LSM was run at 3 different spatial resolutions of 500, 250 and 125 m with a common native temporal QPE resolution for the spatial resolution experiment, and at two different temporal resolutions of 1 and 10 min with a common spatial resolution of 250 m for the temporal resolution experiment. In the above experiments, the resolution of the routing models was fixed at 250 m. The limited number of combinations of resolutions represent a compromise between the computational requirements and the range of resolutions that are most likely to be of operational interest in the study area.

It was observed in the early stages of the spatial resolution experiment that the mean areal precipitation (MAP) calculated at 500 m resolution is significantly different from that at 250 m or 125 m. The differences were traced to the coarseness of 500 m grid boxes in delineating small catchments in WRF-Hydro. Significant errors in precipitation volume often translate into significant errors in peak flow and time-to-peak flow. As such, we excluded 500 m resolution from further consideration. For routing, we initially considered 25 m resolution as well. It was discovered in the early stages, however, that the number of stream segments at this resolution for the study domain exceeds the maximum allowed by WRF-Hydro. For this reason, we excluded 25 m from further consideration for routing. Though limited in number, the resulting combinations allow comparisons of the LSM resolutions of 250 m and 125 m given the common routing model resolution of 125 m and of the routing model resolutions of 250 m, 125 m and 50 m given the common LSM resolution of 125 m.

3.2 Calibration

WRF-Hydro employs a large number of parameters for rainfall-runoff and routing modeling. Most of them are modeled as spatially-varying and specified by spatial maps or lookup tables of the relevant physiographic variables. Due to the computational cost, it is impractical to calibrate a large number of parameters. The approach taken in this work is to identify only the most influential and adjust them up or down with multiplicative scaling factors over the entire catchment, thus maintaining the prescribed spatial variations and physiographic relationships (Gupta et al. 2003). Examination of the model physics described in Eqs. (1) through (10) indicates the most influential parameters for the rainfall-runoff and routing models are likely to be the potential infiltration rate decay coefficient k in Eq. (2), the Manning's friction coefficient for overland flow, n_{ov}, in Eq. (7) and the 4 channel routing parameters of the Manning's friction coefficient n, the bottom width, B_w, the side slope z, and the initial water depth, h. The above 6 parameters, k, n_{ov}, n, B_w, z and h, are denoted in WRF-Hydro as $refdk,\ sfc\_rough, rmannn$, bw, $chsslp$ and $hlink$, respectively, which are used below. Extensive sensitivity analysis involving all rainfall-runoff and routing parameters confirm the above choices. The decay coefficient k in Eq.(2) is coded in WRF-Hydro as:

$$k = \left(\mathrm{REFKDT}\frac{DKSAT}{REFDK}\right) \cdot \left(\frac{DT}{86400}\right) \tag{11}$$

where $DKSAT$ denotes the saturated hydraulic conductivity, $REFDKDT$ and $REFDK$ are parameters for surface runoff (Gochis et al. 2018), and DT denotes the time step in seconds. Both $REFKDT$ and $REFDK$ are calibratable parameters. Because adjusting $REFDKT$ has the same effect as adjusting $REFDK^{-1}$ for k, it is not necessary in practice to calibrate both. As such, we calibrate only $REFDK$ in this work. Note in Eq. (11) that, if $REFDK$ increases or decreases, k decreases or increases and hence the infiltration capacity decreases or increases given the maximum water holding capacity, D_x, respectively. Accordingly, one may consider $REFDK$ as controlling the runoff ratio. All other parameters in the LSM are set to the WRF-Hydro default (Gochis et al. 2018).

For the terrain routing model, n_{ov} is by far the most important. In WRF-Hydro, n_{ov} is prescribed according to the USGS 24-category land cover (Loveland et al. 1995). In this work, we use the National Land Cover Database (NLCD, Wickham et al. 2019) and the same default land cover-dependent values of n_{ov}. In the calibration process, we apply a single multiplicative adjustment factor to the spatially varying n_{ov} for the entire catchment. Calibration of channel routing parameters presents a particular challenge as elaborated below. There are a total of 4 parameters, B_w, z and n, and the initial condition, h, to be determined in the calibration process whereas the only source of information available is observed streamflow at the catchment outlet. For most natural channels, the cross sections are not trapezoidal. It is hence difficult to prescribe B_w and z externally based on physiographic information particularly for small streams. Given the above picture, we opted to assess first the impact of changes in each channel routing parameter via a series of idealized sensitivity analysis using the recently developed general analytical solution for nonlinear reservoir (Nazari and Seo 2020). In this analysis, we prescribe an impulse as the upstream hydrograph and route it through a nonlinear reservoir which is modeled as a hydraulically-equivalent trapezoidal channel as in WRF-Hydro. We then visually examine the shape of the downstream hydrographs and assess the impact of changes in each of the 4 parameters to the downstream hydrograph. The results indicate that changes in each of the 4 routing parameters often produce similar effects, that the shape of the outlet hydrograph is least sensitive to changes in z and that, in addition to n, both B_w and h shape the outlet hydrograph to a significant degree, in particular, the upper and lower parts of the falling limb. The above findings suggest that one may be able to prescribe z externally and calibrate only the other three. In this work, we chose to calibrate all 4 parameters to assess empirically the degree of under-determinedness in each.

For calibration, we initially considered the Shuffled Complex Evolution (SCE, Duan et al. 1992) and the Stepwise Line Search (SLS, Kuzmin et al. 2008). Due to excessive computational requirement of SCE, however, we chose SLS as the main calibration technique (see Kuzmin et al. 2008 for comparison). Once the parameter space is defined, we use Latin Hypercube sampling (LHS, Tang 1993) to run WRF-Hydro with the randomly-sampled parameter values from which a small number of best-performing parameter sets is retained. We then run SLS using the parameter sets retained above as starting points, visually examine the resulting hydrographs and choose the best. The original SLS minimizes the multi-scale objective function consisting of normalized root mean square error of simulated flow at multiple time scales of aggregation such as hourly, daily, weekly, monthly, etc. The hydrologic response time of the study basins, on the other hand, is sub-daily for which the multiscale objective function is not necessary. A second modification to SLS deals with the objective function itself as elaborated below. Arguably the two most important variables for urban flood prediction are the peak flow and time-to-peak flow, i.e., the time until the peak flow occurs relative to some reference time of user's interest. The hydrographs for the study basins are often characterized by high degrees of peakedness due to fast surface runoff over urban and semi-dry land surfaces. Commonly used objective functions for calibration such as the mean squared error (MSE) of simulated flow or its variable transform is not very effective in simulating very sharp peaks due to the typically very small number of observations associated with peak flows. To address the above, we combine the mean error (ME), MSE and Type II conditional bias (CB) for the objective function as follows the last of which is specifically to improve simulation of peaked hydrographs:

$$J = \left(\frac{1}{n}\Sigma_{i=1}^{n} O_i - \frac{1}{n}\Sigma_{i=1}^{n} S_i\right)^2 + \frac{1}{n}\sum_{i=1}^{n}(O_i - S_i)^2$$

$$+\alpha \frac{1}{n} \sum_k^K n_k \left\{ O_k^{mid} - \frac{1}{n_k} \sum_{i=1}^{n_k} \left(S_i | O_k^{min} \le O_i \le O_k^{max} \right) \right\}^2 \quad (12)$$

where O_i and S_i denote the observed and simulated flows at timestep i, n denotes the total number of $\{O_i, S_i\}$ pairs in the calibration period, α denotes the weight given to the conditional bias penalty term, K denotes the number of subintervals dividing the range of observed flow, O_k^{min} and O_k^{max} denote the lower and upper bounds of the k-th subinterval, n_k denotes the number of observed flow within the k-th subinterval, O_k^{mid} denotes the mid-point between O_k^{min} and O_k^{max}, i.e., $O_k^{mid} = O_k^{min} + (O_k^{max} - O_k^{min})/2$, and $S_i | O_k^{min} \le O_i \le O_k^{max}$ denotes the i-th simulated flow for which the verifying observed flow falls in the k-th subinterval. The three terms in Eq. (12) represent the ME, the MSE and the mean of the Type-II CB squared, respectively. The first term may appear redundant in that reducing CB is a sufficient condition for reducing ME. In practice, however, the CB penalty may not be effective across all ranges of flow due to small sample size in certain sub-ranges. Our experience indicates that a sub-range of 10 (cms) and $\alpha = 2$ generally yield satisfactory results for the study basins. We note here that the last two terms in Eq. (12) represent a sample statistic for the objective function used in CB-penalized optimal linear estimation for improved estimation of extremes (Brown and Seo, 2013; Seo, 2012; Seo et al., 2014; Kim et al., 2016, Seo et al., 2018a,b; Shen et al., 2019, Lee et al. 2019, Jozaghi et al. 2019).

Though the number of parameters calibrated is small, it is still computationally too expensive to perform resolution-specific calibration for all combinations of resolutions (see Table 2). The alternative strategy adopted in this work is to calibrate using SLS-LHS at the lowest spatial resolution, i.e., 250 m for both the LSM and routing models, and use the resulting parameter values as the starting point for calibration at the next higher-resolution using SLS only.

For the routing model resolution of 50 m, however, the above strategy could not be used due to excessively large computational requirements (see Table 3). Instead, we borrow the calibration results at 250 m LSM and 125 m routing models and assess parameter transferability from 125 m to 50 m for routing. Event-specific calibration is bound to overfit the specific event at hand. To avoid dependent evaluation based on overfitted parameters, we averaged the middle 3 parameter values out of the 5 from event-specific calibration. The rationale for dropping the largest and the smallest values is to avoid large biases arising from possible extremes. The average parameter values thus obtained are referred to as the non-event-specific calibration results.

3.3 Assimilation of streamflow observations

Hydrologic and hydraulic processes are heavily controlled by complex local physiography. The models may not capture the fixed boundary conditions, the ICs or the physical processes occurring over certain ranges of scale. In addition, the precipitation input may have significant systematic or random errors, or the hydrologic model may lack adequate calibration. In such situations, the model states may become too unrealistic to produce skillful predictions especially when the hydrometeorological or hydrologic conditions depart from the historically observed. For this reason, some form of state updating, manual or automatic, is generally necessary for real-time flood forecasting (WMO 1992). With high-resolution models, however, manual DA is not viable due to the very large dimensionality (Lee et al. 2011, 2014). In this work, we assess how assimilating streamflow observations at the catchment outlet may be used to initialize WRF-Hydro for event-based prediction. For the DA method, we use the fixed-lag formulation (Seo et al. 2003, 2009) of the ensemble Kalman filter (EnKF, Evensen 1994, 2003). The motivation for the fixed-lag smoother is to support forecaster-supervised on-demand initialization of WRF-

Hydro whether DA was previously run or not. We note here that EnKF is implemented in OpenDA (Van Velzen et al. 2016, Rakovec et al. 2015) which is integrated with the NWS's Community Hydrologic Prediction System (Roe et al. 2010), the main operational river forecast system at the RFCs. As such, there already exists an operational tool for implementation of the proposed method.

The control variables, i.e., the variables to be updated or adjusted via DA, include the multiplicative adjustment factor, β_P, to precipitation, P_x, applicable uniformly to the precipitation over the entire catchment P_x, and over the entire assimilation window (see Eq. (13)), and the multiplicative adjustment factor, β_θ, to soil moisture, β_θ, applicable uniformly to all 4 soil moisture layers $\theta_i, i = 1,..,4$, and valid at the beginning of the assimilation window(see Eq. (14)):

$$Q_s = \frac{(\beta_P P_x)^2}{(P_x+I_c)^2}, \ \beta_P \geq 0 \qquad (13)$$

$$D_x = \sum_{i=1}^{4} \Delta Z_i(\theta_{sat} - \beta_\theta \theta_i), \ \beta_\theta \geq 0, i = 1,..,4 \qquad (14)$$

The simulated streamflow observations are then augmented to the state vector to render the observation equation linear (Lorentzen and Nævdal 2011, Rafieeinasab et al. 2014, Lee et al. 2019). As formulated above, the DA problem amounts to solving for the two adjustment factors in each assimilation cycle such that the simulated streamflow at the catchment outlet tracks the observed. If sequential estimation is desired, the control variables may be propagated from one assimilation cycle to the next based, e.g., on the first-order autogressive-1 model (Lee et al. 2019). Different variations of the above DA approach have been used successfully with both lumped and distributed hydrologic models in both operational and research settings in the US and elsewhere (Lee et al. 2011, Lee et al. 2012, Lee and Seo 2014, Lee et al. 2015, 2016, Kim et al. 2014, Mazzoleni et al. 2019, Noh et al. 2018, Rafieeinasab et al. 2014, Riazi et al. 2016, Seo et al. 2003, 2009).

An important difference between the above formulation and the previous formulations of fixed lag smoothing is that the former does not include additive errors to runoff, i.e., later inflow into channels. The reason for this departure is that the addition requires modifications to the WRF-Hydro source code. Because there is no guarantee a priori that the model dynamics admit the error-added flows, the above modifications may produce numerical instabilities that are difficult to diagnose or control. The lack of additive error in the control vector means that the DA formulation is strongly-constrained rather than weakly-constrained (Lee et al. 2016), and hence more likely to render the smoother more susceptible to model structural or parametric errors. In addition to the assimilation window length and ensemble size, it is necessary to prescribe several uncertainty parameters for the smoother: the observation error variances for precipitation and streamflow, and mean and variance (or, alternatively, median and coefficient of variation) of each of β_θ and β_p. In this work, the above DA parameters were prescribed following Lee et al. (2019) using the homoscedastic model and lognormal distribution for β_θ and β_p, and were estimated based on limited sensitivity analysis (Rafieeinasab et al. 2015, Lee et al. 2019). Due to the strongly-constrained nature of the DA formulation, however, the performance of DA is likely to benefit significantly from more rigorous estimation of the DA parameters.

4 Results

Our assessment consisted of the 5 experiments described below. We use peak flow and time-to-peak flow errors as the primary performance measures, by far the two most important for urban flood prediction (Liu et al. 2011, Rafieeinasab et al. 2014).

4.1 Experiment 1: Event-specific vs. non-event-specific calibration

Fig 3 shows examples of event-specific (black) vs. non-event-specific (red) calibration results at 250 m resolution for both the LSM and routing models. Additional results are presented in Fig 10 in the context of DA. The temporal resolution of QPE is 1 min. The event-specific results are based on calibrating the 6 parameters specifically for each event. The non-event-specific results are based on dropping the largest and smallest values from the 5 event-specific results and averaging only the middle 3. It is important to point out that, in event-specific calibration, $rekft$ reflects the soil moisture ICs. Note in Eqs. (2) and (4) that changing $refdk$ has effects similar to changing the maximum water holding capacity of the soil, D_x, which is a function of the initial soil water content. Event-specific calibration of $refdk$ is hence subject to event-to-event variability of antecedent soil moisture conditions. The averaging of the 3 middle parameter values from the event-specific results is an attempt to dampen or average out this variability in the ICs. To illustrate, Fig 4a shows the event-specific result for the multiplicative factor to $rmannn$, or fac_rmannn. Significant event-to-event variations are seen particularly for less impervious CC and FC (see Fig 1). Fig 4b shows the non-event-specific result from averaging the middle 3 parameter values in Fig 4a. Note that JC, which has the largest impervious fraction (see Fig 1), has significantly smaller $rmannn$ than CC and FC, and that little adjustment from the WRF-Hydro default was needed for the least impervious FC.

The event-specific results indicate that the calibration strategy is mostly successful in simulating hydrographs for the most important rising limbs. For a number of cases, however, the simulated hydrographs do not recede as quickly as the observed. A likely contributing factor is that WRF-Hydro does not model storm drains. While the impact of storm drains is not very significant for large events (Rafieeinasab et al. 2015), in lower flow conditions, the impact is likely to be larger (Habibi and Seo 2018). Of the 15 cases (i.e., from 5 events for 3 basins), significant differences were observed for 10 cases between the event-specific and non-even-specific results. Comparison of the parameter values between the two indicates that significant differences exist most often in $refdk$ followed by $rmannn$ and sfc_rough. For bw, $hlink$ and $chsslp$, significant differences were observed only in a few cases. The large event-to-event variability of $refdk$ is not surprising in that in event-specific calibration this parameter can effectively control dynamically-varying runoff ratio as explained above. Of the 15 non-event-specific cases, 6 and 3 cases show over- and under-simulation of runoff volume resulting in over- and under-simulation of peak flows and too early and late rises to peak flows, respectively. Fig 5a shows the simulated peak flows from event-specific (black) and non-event-specific (red) calibration vs. the observed. Fig 5b shows the associated time-to-peak flow since the beginning of the rising limb vs. the observed. In Fig 5b, the absolute magnitude of the time-to-peak flow is of little importance because the beginning of the rising limb can be anywhere, and only the departure of the time-to-peak flow from the diagonal is of interest. In Fig 5, the JC Feb 2018 event was excluded due to lack of observed peak flow. Shown for reference in Fig 5a and Fig 5b are the lines of 10, 20 and 30 percent errors in peak flow and of 1, 2 and 3 hr errors in time-to-peak flow, respectively. Harmel et al. (2006) report streamflow measurement errors of 42%, 19%, 10%, 6% and 3% for small watersheds for the worst, typical maximum, typical average, typical minimum, and the best case scenarios, respectively. Di Baldassarre and Montanari (2009) report that the overall error affecting river discharge observations ranges from 6.2% to 42.8%, at the 95% confidence level, with an average value of 25.6%. The 10 to 30 percent error lines in Fig 5a hence provide a sense of the magnitude of the errors in simulated peak flow relative to possible observational errors. Empirical unit hydrographs for JC, CC and FC show time-to-peak values of 0.75, 3 and 2.75 hrs, respectively (Rafieeinasab et al. 2015). An error in time-to-peak flow on the order of the time-to-peak values hence indicates poor performance. Fig 5 indicates that most case-specific calibration results have less than 10% error in peak flow and less than an hour of time-to-peak flow error, but that, for about 5 cases, the non-event-specific results suffer from significantly larger errors. All 5 cases of excessively large peak flow or time-to-peak flow errors are associated with significant volume errors except for the FC May 2019 case for which a less than accurate simulation of the rising limb is responsible for the large time-to-peak flow error. The above results indicate that high-quality initialization is necessary for event-based urban flood prediction using WRF-Hydro. In Experiment 5, we assess how DA may help address the situation.

4.2 Experiment 2: Impact of temporal resolution of precipitation

In this experiment, we assess how the temporal resolution of precipitation input may impact the quality of streamflow simulation by forcing the LSM with 1-min average of 10-min QPE vs. the native 1-min QPE. For 10 min QPE, we aggregate the 1-min CASA QPE to 10 min accumulations and run the LSM at 1 min timestep using the 1-min average over each 10 min period. For comparison, we also ran the LSM at 10 min timestep using 10-min QPE. In this experiment, we use the parameter values obtained from the event-specific calibration to reduce hydrologic uncertainty. The common spatial resolution used is 250 m for both the LSM and routing models. Examination of the results for all cases indicates that the differences in simulated hydrographs due to 1 min vs. 10 min QPE are very small except for the May 2019 event which we elaborate below. Fig 6 shows the simulated vs. observed hydrographs at the outlet of JC for the May 2019 event. The simulation of the second rise for this double-peaked event is cut short due to missing CASA QPE. To identify possible causes for the disparate response in simulated streamflow, we examined the MAP time series for all cases. It is observed that the MAP values for the second peak of the May 2019 event are significantly smaller than those for all other events. Because runoff generation may be considered as thresholding rainfall such that little runoff occurs for rain rate below some threshold and almost all excess rainfall runs off for rain rate above the threshold (see Subsection 2.4, Norouzi et al. 2019), one may look for a threshold rain rate above and below which the runoff response is very different. Examination of the MAP hyetographs and the associated hydrographs for the May 2019 event points to a threshold of about 0.5 mm. For this event, the maximum 1 min MAP associated with the second peak was well above 0.5 mm for all three basins. The maximum 1 min-average of 10 min MAP, on the other hand, was well below 0.5 mm for JC and CC, and stayed above 0.5 mm only for a single 10 min period for FC. The above findings indicate that the SWB used for rainfall-runoff modelling in WRF-Hydro is sensitive to the temporal resolution of precipitation for moderate precipitation amounts due to the increased nonlinearity in runoff generation (see Eqs. (1), (2) and (11)).

4.3 Experiment 3: Impact of spatial resolutions of rainfall-runoff modelling and routing

In this experiment, we compare the quality of the outlet simulations for peak flow and time-to-peak flow among the resolutions of 250 m, 125 m and 50 m for routing with a common LSM resolution of 125 m, and between the resolutions of 250 m and 125 m for LSM with a common routing model resolution of 125 m. The 250 m LSM and 250 m routing model simulations, referred to herein as the 250m-250m results, are based on event-specific calibration using SLS with LHS. One may hence consider the above calibration as based on quasi-global optimization.

The 250 m LSM and 125 m routing simulations, referred to herein as the 250m-125m results, are based on event-specific calibration using only SLS in which the local search is started with the 250m-250m results. One may hence consider the above calibration as local optimization of a priori parameter values from a coarser resolution. As mentioned in Section 3, it was not possible to calibrate at the 250 m LSM and 50 m routing resolution due to excessive computational requirements (see Table 3). The 250 m LSM and 50 m routing simulations, referred to herein as the 250m-50m results, are based on the parameter values borrowed from the 250m-125m results. One may hence consider the above results as based solely on a priori parameter values transferred from a coarser resolution. Because the level of calibration is different from one resolution to another, it is not very meaningful to compare the non-event-specific results. For this reason, we focus below on the event-specific results only.

Fig 7a and 7b show the simulated peak flow vs. the observed, and the simulated time-to-peak flow vs. the observed, respectively. As in Fig 5, we overlay the 10, 20 and 30 percent error lines in Fig 7a and of 1, 2 and 3 hours of timing error lines in Fig 7b to help assess the magnitude of the errors. Fig 7 indicates that the 250m-250m and 250m-125m results, both of which are calibrated scale-specifically, are very similar, and that for a number of events the 250m-50m results are not as good as the above two. The above observations are perhaps not very surprising in that one may expect scale-specific calibration to perform better than using parameter values borrowed from a lower resolution. The magnitude of the errors in the 250m-50m results, however, is surprisingly large for a number of events. To trace the potential sources of the error, we examined the spatially-distributed channel routing parameters, including the channel grid, flow accumulation, flow direction and stream order at all resolutions. It is seen that, whereas the differences between 250 and 125 m are relatively small, there are large differences between 50 m and the coarser resolutions. To illustrate, Figs 8a and 8b show the histograms of the stream order in the model domain at resolutions of 125 m and 50 m, respectively. The histogram at 250 m is similar to that at 125 m. In the figure, the frequency for the stream order of zero represents the number of grid boxes that do not contain any channel segments. As one may expect, at 50 m resolution, the channel network is much denser and has more higher-order streams. WRF-Hydro prescribes the channel routing parameters according to the stream order. As such, changes in the channel density or stream order are very likely to change the conveyance characteristics of the channel network. The above findings suggest that a combination of resolution-specific prescription of the channel routing parameters and their calibration is likely to be necessary to benefit from very high-resolution modeling using WRF-Hydro. We also compared the 250m-125m results with the 125m-125m to assess the impact of increasing the LSM resolution. As with the 250m-125m results, the 125m-125m results are based on scale-specific local optimization using SLS in which the parameter values from the 250m-125m results are used as the starting point. The comparison indicates that the 125m-125m results improve the peak flow prediction over the 250m-125m for the study basins but only marginally.

4.4 Experiment 4: Impact of quality of ICs

In this experiment, we assess how the quality of the ICs of the rainfall-runoff model may impact the accuracy of streamflow prediction. A potential source of the ICs in real-time event-based operation of WRF-Hydro is the warm states of the NWM. A direct use in this experiment of the NWM warm states, however, is not likely to allow clear attribution at least for two reasons. The first is that the USGS 24-category land cover (see Fig 1c) and the MRMS QPE (Zhang et al. 2011, 2016) used in NWM are of coarser resolution than those used in this work. The second is that the model parameter values used in the NWM (Gochis et al. 2019) are not the same as those used in WRF-Hydro in this work. As such, the ICs from the NWM analysis are not likely to transfer cleanly to WRF-Hydro as implemented in this work as evidenced in Experiments 1 through 3 above. As a compromise, we emulate the NWM analysis by running WRF-Hydro using the USGS 24-category land cover and NLDAS precipitation (Cosgrove et al. 2003) in place of the NLCD land cover and CASA QPE, respectively. The NLDAS precipitation has a much lower resolution than the 1 km 1 hr MRMS QPE used by the NWM. It is hence possible that the results from this experiment may somewhat inflate the positive impact of higher resolution precipitation. The above experiment design nonetheless completely removes all model-parametric uncertainties and hence makes possible unambiguous attribution.

In this experiment, we start running WRF-Hydro at least several hours before the prediction time using the NLDAS precipitation and USGS 24-category land cover where the lower resolution NLDAS precipitation is disaggregated uniformly in space and time to a resolution of 250 m and 1 min. The prediction time is chosen where the observed hydrograph begins to rise. This is also when streamflow response is most sensitive to the ICs. At the prediction time, we switch to the CASA QPE and NLCD land cover for simulation over the forecast horizon. For the above comparison run, we assume average soil moisture conditions for the LSM and pre-storm conditions for the hillslopes and channel routing models as obtained from event-specific calibration (see Subsection 4.1). In the baseline run, we run the model at 250 m 1 min resolution using the CASA QPE and NLCD land cover for the entire simulation period. Any differences in the two simulated hydrographs over the forecast horizon are hence due solely to the ICs valid at the prediction time. Fig 9a shows the simulated vs. observed peak flow for the NLCD (black) and USGS 24-category (red) land cover. All other conditions are the same as in the baseline

250m-250m simulation. The positive impact of higher-resolution land cover is readily seen. Note that the differences are the smallest for JC which is identified mostly as urban by the USGS 24-category land cover in agreement with the NLCD (see Fig 1c,d). Fig 9b shows the simulated vs. observed peak flow for the CASA (black) and NLDAS (red) QPE-forced ICs. All other conditions are the same as in the baseline 250m-250m simulation. Note the very significant positive impact of higher-resolution QPE, particularly for CC and FC for Feb 2018 and Sep 2018, the two largest events among the five (see Fig 2 and Table 1). Examination of timing errors associated with Figs 9a and 9b shows similarly positive impact of higher-resolution QPE and, to a lesser extent, land cover.

4.5 Experiment 5: Impact of updating ICs via DA

In this Experiment, we assess how DA may potentially be used to initialize WRF-Hydro for event-based prediction. In the real world, it is generally not possible to schedule pre-storm warmup runs as described in the 4^{th} Experiment. Instead, it is necessary to be able to initialize the model on demand often without the aid of any a priori information. The fixed-lag smoother, solved using EnKF in this work, is aimed at supporting such an operation. For high-resolution runs, EnKF is computationally expensive. In this work, all ensemble runs were made at the coarsest spatial resolution of 250 m for both the LSM and routing models. Limited sensitivity analysis suggests that a small ensemble size of 12 is generally acceptable for ensemble mean prediction owing to the very low dimensionality of the DA formulation. We then use the non-event-specific calibration results to emulate realistic model-parametric uncertainty and predict streamflow with and without DA. Due to the small sample size, quantitative verification was not possible. Instead, we critically examine the DA-aided predictions for those 5 cases for which the non-event-specific calibration results compare least favorably with the event-specific in Experiment 1 (see Fig 3). By far the largest potential value of DA in urban flood prediction is improving peak flow and time-to-peak flow predictions when the streams first respond to rainfall. Accordingly, we focus specifically on DA-aided predictions when the hydrograph begins to rise. This is also the time when the degrees of freedom for signal for DA (Rodgers 2000) is greatly reduced due to the generally reduced predictive skill of rainfall-runoff and routing models, and hence streamflow observations carry larger information content relative to the model prediction (Zupanski et al. 2007, 2009).

Fig 10 shows the streamflow predictions without DA (red), DA-aided ensemble predictions (cyan), the associated ensemble mean predictions (blue), ensemble streamflow analysis from DA (green) and the verifying observed hydrographs (empty blue circles) for 4 of the 5 cases for which non-event-specific calibration produced very poor simulations in Experiment 1. The case not shown in Fig 10 due to space limitations is JC Apr 2019 which is by far the smallest event of the 5 and is hence of lesser interest. In the figure, the vertical gray line indicates the prediction time which also marks the end of the assimilation window. The horizontal extent of the ensemble analysis (green) shows the size of the assimilation window. All streamflow and precipitation observations valid within the assimilation window are assimilated in these runs to update the soil moisture states valid at the prediction time. All DA results are based on single assimilation cycles to emulate on-demand operation without the potential benefit of any previous DA cycles. The results indicate that DA improves prediction for all 5 cases over the DA-unaided base predictions. For the FC Jan 2017 and CC Feb 2018 events, for which non-event-specific calibration very significantly over- and under-predict, respectively, DA greatly improves prediction. As noted in Section 3, the primary source of error in peak flow or time-to-peak flow is the error in runoff volume. The results indicate that DA is largely able to reduce runoff volume errors by providing WRF-Hydro with high quality ICs. Fig 10 shows, however, that the ensembles are significantly underspread in the recession limb due to lack of accounting of structural and parametric uncertainties, and that WRF-Hydro is not able to reproduce the bimodal or attenuated peaks, or the fast-receding falling limbs in FC Jan 2017 (Fig 10a) and FC Feb 2018 (Fig 10c). The above results indicate that, overall, the fixed-lag smoother is very effective in reducing runoff volume errors and hence errors in peak flow and time-to-peak flow.

5 Conclusions and future research recommendations

We assess the impact of increasing the resolution of hydrologic modeling, calibration of selected model parameters and assimilation of streamflow observations toward event-based high-resolution urban flood modeling and prediction using WRF-Hydro in the Dallas-Fort Worth area (DFW). We use quantitative precipitation estimates (QPE) at 500-m 1-min resolution from the Collaborative Adaptive Sensing of the Atmosphere (CASA) operation for observed rainfall, the Stepwise Line Search for calibration, and ensemble Kalman filter (EnKF) implementation of fixed-lag smoothing for data assimilation (DA). The model domain is a 144.6 km^2 area comprising 3 urban catchments in the Cities of Arlington and Grand Prairie in the middle of DFW. The main findings, conclusions and recommendations follow below.

Event-specific calibration of the 6 WRF-Hydro parameters identified in this work is largely successful in simulating hydrographs in the study area, in particular, the most important rising limbs. It is less successful, however, for attenuated peaks or fast-receding falling limbs. A novel element in the above calibration is the inclusion of a conditional bias penalty in the objective function to improve simulation specifically of highly peaked hydrograph. A spatial resolution of at least 250 m is necessary for the land surface model (LSM) to delineate small catchments and hence to capture catchment-wide rainfall with acceptable accuracy. Increasing the resolution of the LSM from 250 m to 125 m showed marginal improvement. The same resolution increase for the routing models showed little improvement. Increasing the routing resolution further to 50 m using parameter values borrowed from 125 m, on the other hand, increased errors for a number of cases due to large changes in channel grid and stream order. The above findings suggest that, to benefit from very high-resolution modeling using WRF-Hydro, a combination of resolution-specific prescription and calibration of the channel routing parameters is likely to be necessary. The high-resolution CASA QPE and the National Land Cover Database (NLCD) land cover showed very significant and significant positive impact on streamflow simulation compared to the lower-resolution North American Land Data Assimilation System (NLDAS) QPE and USGS 24-category land cover, respectively. The above points out the importance of resolution-consistent high-quality initialization of WRF-Hydro for event-based operation. The EnKF implementation of fixed-lag smoother significantly reduced peak flow errors under realistic parametric uncertainty for predictions made when streams first respond to rainfall. The DA-aided ensemble predictions are, however, significantly underspread in the recession limb due to lack of accounting of structural and parametric uncertainties. The overall results suggest that, in the absence of resolution-specific prescription and calibration of channel routing parameters, a resolution of 250 m for both the LSM and routing models is a good choice in terms of performance and computational requirements. Recall that the National Water Model currently runs routing at 250 m over the continental US. The results also suggest that, in the absence of high-quality calibration and continuous simulation of streamflow, DA is necessary to initialize WRF-Hydro for event-based operation for high-resolution urban flood prediction.

Acknowledgements

This material is based upon work supported in part by the NOAA's Joint Technology Transfer Initiative Program (JTTI) under Grants NA170AR4590174 and NA17OAR4590184, and by NSF under Grant CyberSEES-1442735. These supports are gratefully acknowledged. We would like to thank the NWS Collaborators for the second JTTI project, Dr. Michael Smith of NOAA/NWS/Office of Water Prediction and Mr. Ernie Wells of NOAA/NWS/Analyze, Forecast, and Support Office for valuable input and assistance throughout the course of the project.

References

Akan, A.O., Houghtalen, R.J., 2013. Urban Hydrology, Hydraulics, and Stormwater Quality: Engineering Applications and Computer Modeling. Wiley, Hoboken.

Alizadeh, B., Limon, R.A., Seo, D.-J., Lee, H., Brown, J., 2020. Multiscale postprocessor for ensemble streamflow prediction for short to long ranges. Journal of Hydrometeorology 21, 265–285. https://doi.org/10.1175/JHM-D-19-0164.1

Brown, J.D., Seo, D.-J., 2013. Evaluation of a nonparametric post-processor for bias correction and uncertainty estimation of hydrologic predictions. Hydrological Processes 27, 83–105. https://doi.org/10.1002/hyp.9263

Chandrasekar, V., 2017. The CASA Dallas-Fort Worth urban radar network for flood monitoring: accomplishments and lessons learned after 4 years of operation. Presented at the Weather Radar and Hydrology, Seoul, Korea.

Chandrasekar, V., Chen, H., Philips, B., Seo, D., Junyent, F., Bajaj, A., Zink, M., McEnery, J., Sukheswalla, Z., Cannon, A., Lyons, E., Westbrook, D., 2013. The CASA Dallas-Fort Worth remote sensing network ICT for urban disaster mitigation 15, EGU2013-6351.

Chandrasekar, V., Wang, Y., Chen, H., 2012. The CASA quantitative precipitation estimation system: a five year validation study. Natural Hazards and Earth System Sciences 12, 2811–2820. https://doi.org/10.5194/nhess-12-2811-2012

Chen, H., Chandrasekar, V., 2015. The quantitative precipitation estimation system for Dallas–Fort Worth (DFW) urban remote sensing network. Journal of Hydrology, Hydrologic Applications of Weather Radar 531, 259–271. https://doi.org/10.1016/j.jhydrol.2015.05.040

Chen, H., Lim, S., Chandrasekar, V., Jang, B.-J., 2017. Urban hydrological applications of dual-polarization x-band radar: case study in Korea. Journal of Hydrologic Engineering 22, E5016001. https://doi.org/10.1061/(ASCE)HE.1943-5584.0001421

Cifelli, R., Chandrasekar, V., Chen, H., Johnson, L.E., 2018. High resolution radar quantitative precipitation estimation in the San Francisco Bay area: rainfall monitoring for the urban environment. Journal of the Meteorological Society of Japan 96A, 141–155. https://doi.org/10.2151/jmsj.2018-016

Cosgrove, B.A., Lohmann, D., Mitchell, K.E., Houser, P.R., Wood, E.F., Schaake, J.C., Robock, A., Marshall, C., Sheffield, J., Duan, Q., Luo, L., Higgins, R.W., Pinker, R.T., Tarpley, J.D., Meng, J., 2003. Real-time and retrospective forcing in the North American Land Data Assimilation System (NLDAS) project. Journal of Geophysical Research: Atmospheres 108, 2002JD003118. https://doi.org/10.1029/2002JD003118

Di Baldassarre, G., Montanari, A., 2009. Uncertainty in river discharge observations: a quantitative analysis. Hydrology and Earth System Sciences 6. https://doi.org/10.5194/hessd-6-39-2009

Duan, Q., Sorooshian, S., Gupta, V., 1992. Effective and efficient global optimization for conceptual rainfall-runoff models. Water Resources Research 28, 1015–1031. https://doi.org/10.1029/91WR02985

Evensen, G., 1994. Sequential data assimilation with a nonlinear quasi-geostrophic model using Monte Carlo methods to forecast error statistics. Journal of Geophysical Research: Oceans 99, 10143–10162. https://doi.org/10.1029/94JC00572

Evensen, G., 2003. The ensemble Kalman filter: theoretical formulation and practical implementation. Ocean Dynamics 53, 343–367. https://doi.org/10.1007/s10236-003-0036-9

Gochis, D., Barlage, M., Dugger, A., FitzGerald, K., Karsten, L., McAllister, M., McCreight, J., Mills, J., Rafieei Nasab, A., Read, L., Sampson, K., Yates, D., Yu, W., 2018. The WRF-Hydro modeling system technical description, (Version 5.0). Available online at: https://ral.ucar.edu/sites/default/files/public/WRF-HydroV5TechnicalDescription.pdf. (last accessed: Jul 07, 2020)

Gochis, D., Yates, D., Sampson, K., Dugger, A., McCreight, J., Barlage, M., Rafieeinasab, A., Karsten, L., Read, L., Zhang, Y., McAllister, M., Cabell, R., FitzGerald, K., 2019. Overview of national water model calibration general strategy & optimization.

Graziano, T., Clark, E., Cosgrove, B., Gochis, D., 2017. Transforming National Oceanic and Atmospheric Administration (NOAA) water resources prediction. Presented at the 97th American Meteorological Society Annual Meeting, AMS, Seattle, WA.

Green, W.H., Ampt, G.A., 1911. Studies on Soil Phyics. The Journal of Agricultural Science 4, 1–24. https://doi.org/10.1017/S0021859600001441

Gupta, H.V., Sorooshian, S., Hogue, T.S., Boyle, D.P., 2003. Advances in automatic calibration of watershed models, in: Calibration of Watershed Models. American Geophysical Union (AGU), pp. 9–28. https://doi.org/10.1029/WS006p0009

Habibi, H., Dasgupta, I., Noh, S., Kim, S., Zink, M., Seo, D.-J., Bartos, M., Kerkez, B., 2019. High-resolution hydrologic forecasting for very large urban areas. Journal of Hydroinformatics, 21, 441–454. https://doi.org/10.2166/hydro.2019.100

Habibi, H., Rafieeinasab, A., Norouzi, A., Nazari, B., Seo, D.-J., Muttiah, R., Davis, C., 2016. High resolution flash flood forecasting for the Dallas-Fort Worth Metroplex. Journal of Water Management Modeling. https://doi.org/10.14796/JWMM.C401

Habibi, H., Seo, D.-J., 2018. Simple and modular integrated modeling of storm drain network with gridded distributed hydrologic model via grid-rendering of storm drains for large urban areas. Journal of Hydrology 567, 637–653. https://doi.org/10.1016/j.jhydrol.2018.10.037

Harmel, R.D., Cooper, R.J., Slade, R.M., Haney, R.L., Arnold, J.G., 2006. Cumulative uncertainty in measured streamflow and water quality data for small watersheds. Transactions of the ASABE 49, 689–701. https://doi.org/10.13031/2013.20488

Horton, R.E., 1941. An Approach Toward a Physical Interpretation of Infiltration-Capacity. Soil Science Society of America Journal 5, 399–417. https://doi.org/10.2136/sssaj1941.036159950005000C0075x

Jozaghi, A., Nabatian, M., Noh, S., Seo, D.-J., Tang, L., Zhang, J., 2019. Improving multisensor precipitation estimation via adaptive conditional bias–penalized merging of rain gauge data and remotely sensed quantitative precipitation estimates. Journal of Hydrometeorology 20, 2347–2365. https://doi.org/10.1175/JHM-D-19-0129.1

Kean, J.W., Smith, J.D., 2004. Flow and boundary shear stress in channels with woody bank vegetation. Riparian vegetation and fluvial geomorphology 8, 237–252.

Kean, J.W., Smith, J.D., 2005. Generation and verification of theoretical rating curves in the Whitewater River basin, Kansas. Journal of Geophysical Research: Earth Surface 110. https://doi.org/10.1029/2004JF000250

Kean, J.W., Smith, J.D., 2010. Calculation of stage-discharge relations for gravel bedded channels. Journal of Geophysical Research: Earth Surface 115. https://doi.org/10.1029/2009JF001398

Kim, B., Seo, D.-J., Noh, S.J., Prat, O.P., Nelson, B.R., 2018. Improving multisensor estimation of heavy-to-extreme precipitation via conditional bias-penalized optimal estimation. Journal of Hydrology 556, 1096–1109. https://doi.org/10.1016/j.jhydrol.2016.10.052

Kim, S., Seo, D.-J., Riazi, H., Shin, C., 2014. Improving water quality forecasting via data assimilation – Application of maximum likelihood ensemble filter to HSPF. Journal of Hydrology 519, 2797–2809. https://doi.org/10.1016/J.JHYDROL.2014.09.051

Koren, V., Reed, S., Smith, M., Zhang, Z., Seo, D.-J., 2004. Hydrology laboratory research modeling system (HL-RMS) of the US national weather service. Journal of Hydrology 291, 297–318. https://doi.org/10.1016/j.jhydrol.2003.12.039

Kuzmin, V., Seo, D.-J., Koren, V., 2008. Fast and efficient optimization of hydrologic model parameters using a priori estimates and stepwise line search. Journal of Hydrology 353, 109–128. https://doi.org/10.1016/j.jhydrol.2008.02.001

Lee, H., Seo, D.-J., 2014. Assimilation of hydrologic and hydrometeorological data into distributed hydrologic model: Effect of adjusting mean field bias in radar-based precipitation estimates. Advances in Water Resources 74, 196–211. https://doi.org/10.1016/j.advwatres.2014.09.002

Lee, H., Seo, D.-J., Koren, V., 2011. Assimilation of streamflow and in situ soil moisture data into operational distributed hydrologic models: Effects of uncertainties in the data and initial model soil moisture states. Advances in Water Resources 34, 1597–1615. https://doi.org/10.1016/j.advwatres.2011.08.012

Lee, H., Seo, D.-J., Liu, Y., Koren, V., McKee, P., Corby, R., 2012. Variational assimilation of streamflow into operational distributed hydrologic models: effect of spatiotemporal scale of adjustment. Hydrology and Earth System Sciences 16, 2233–2251. https://doi.org/10.5194/hess-16-2233-2012

Lee, H., Seo, D.-J., Noh, S.J., 2016. A weakly-constrained data assimilation approach to address rainfall-runoff model structural inadequacy in streamflow prediction. Journal of Hydrology 542, 373–391. https://doi.org/10.1016/j.jhydrol.2016.09.009

Lee, H., Shen, H., Noh, S.J., Kim, S., Seo, D.-J., Zhang, Y., 2019. Improving flood forecasting using conditional bias-penalized ensemble Kalman filter. Journal of Hydrology 575, 596–611. https://doi.org/10.1016/j.jhydrol.2019.05.072

Lee, H., Zhang, Y., Seo, D.-J., Xie, P., 2015. Utilizing satellite precipitation estimates for streamflow forecasting via adjustment of mean field bias in precipitation data and assimilation of streamflow observations. Journal of Hydrology 529, 779–794. https://doi.org/10.1016/j.jhydrol.2015.08.057

Liu, Y., Brown, J., Demargne, J., Seo, D.-J., 2011. A wavelet-based approach to assessing timing errors in hydrologic predictions. Journal of Hydrology 397, 210–224. https://doi.org/10.1016/j.jhydrol.2010.11.040

Lorentzen, R.J., Naevdal, G., 2011. An iterative ensemble Kalman filter. IEEE Transactions on Automatic Control 56, 1990–1995. https://doi.org/10.1109/TAC.2011.2154430

Loveland, T.R., Merchant, J.W., Brown, J.F., Ohlen, D.O., Reed, B.C., Olson, P., Hutchinson, J., 1995. Seasonal Land-Cover Regions of the United States. Annals of the Association of American Geographers 85, 339–355. https://doi.org/10.1111/j.1467-8306.1995.tb01797.x-i1

Mazzoleni, M., Noh, S.J., Lee, H., Liu, Y., Seo, D.-J., Amaranto, A., Alfonso, L., Solomatine, D.P., 2018. Real-time assimilation of streamflow observations into a hydrological routing model: effects of model structures and updating methods. Hydrological Sciences Journal 63, 386–407. https://doi.org/10.1080/02626667.2018.1430898

Moore, R.B., McKay, L.D., Rea, A.H., Bondelid, T.R., Price, C.V., Dewald, T.G., Johnston, C.M., 2019. User's guide for the national hydrography dataset plus (NHDPlus) high resolution (USGS Numbered Series No. 2019–1096), User's guide for the national hydrography dataset plus (NHDPlus) high resolution, Open-File Report. U.S. Geological Survey, Reston, VA. https://doi.org/10.3133/ofr20191096

Moore, R.J., 1985. The probability-distributed principle and runoff production at point and basin scales. Hydrological Sciences Journal 30, 273–297. https://doi.org/10.1080/02626668509490989

Nazari, B., Seo, D.-J., 2020. Analytical solution for nonlinear reservoir routing with power-law storage function, under review. ASCE Journal of Hydraulic Engineering.

NCAR, 2020. NCAR command language description: ESMF_regrid. Available online at: https://www.ncl.ucar.edu/Document/Functions/ESMF/ESMF_regrid.shtml (last accessed: Jul 07, 2020).

Noh, S. J., Weerts, A. H., Rakovec, O., Lee, H., Seo, D.-J., 2018. Assimilation of streamflow observations, in: Duan, Q., Pappenberger, F., Thielen, J., Wood, A., Cloke, H.L., Schaake, J.C. (Eds.), Handbook of Hydrometeorological Ensemble Forecasting. Springer Berlin Heidelberg, Berlin, Heidelberg, pp. 1–36. https://doi.org/10.1007/978-3-642-40457-3_33-2

Norouzi, A., 2016. Improving Hydrologic Prediction for Large Urban Areas Through Stochastic Analysis of Scale-Dependent Runoff Response, Advanced Sensing and High-Resolution Modeling. University of Texas Arlington.

Norouzi, A., H. Habibi, B. Nazari, S. Noh, D.-J. Seo, Y. Zhang, 2019. Toward parsimonious modeling of frequency of areal runoff from heavy-to-extreme precipitation in large urban areas under changing conditions: a derived moment approach, Stochastic Environmental Research and Risk Assessment, 33(7): 1263–1281. https://doi.org/10.1007/s00477-019-01698

NWS, 2009. Hydrology laboratory-research distributed hydrologic model (HL-RDHM) user manual v. 3.0.0.

NWS, 2020. About the National Water Model [WWW Document]. URL https://water.noaa.gov/about/nwm (accessed 7.13.2020).

Rafieeinasab, A., Norouzi, A., Kim, S., Habibi, H., Nazari, B., Seo, D.-J., Lee, H., Cosgrove, B., Cui, Z., 2015. Toward high-resolution flash flood prediction in large urban areas – Analysis of sensitivity to spatiotemporal resolution of rainfall input and hydrologic modeling. Journal of Hydrology, Hydrologic Applications of Weather Radar 531, 370–388. https://doi.org/10.1016/j.jhydrol.2015.08.045

Rafieeinasab, A., Norouzi, A., Mathew, T., Seo, D.J., Chen, H., Chandrasekar, V., Rees, P., Nelson, B., 2014. Comparative evaluation of multiple radar-based QPEs for North Texas, in: International Symposium Weather Radar and Hydrology. Reston, VA, pp. 7–10.

Rakovec, O., Weerts, A. H., Sumihar, J., Uijlenhoet, R., 2015. Operational aspects of asynchronous filtering for flood forecasting. Hydrology and Earth System Sciences 19, 2911–2924. https://doi.org/10.5194/hess-19-2911-2015

Riazi, H., Kim, S., Seo, D.-J., Shin, C., Kim, K., 2016. Improving operational water quality forecasting with ensemble data assimilation. JWMM. https://doi.org/10.14796/JWMM.C413

Rodgers, C.D., 2000. Inverse Methods for Atmospheric Sounding: Theory and Practice, Series on Atmospheric, Oceanic and Planetary Physics. World Scientific. https://doi.org/10.1142/3171

Roe, J., Dietz, C., Restrepo, P., Halquist, J., Hartman, R., Horwood, R., Olsen, B., Opitz, H., Shedd, R., Welles, E., 2010. NOAA's community hydrologic prediction system, in: Proceedings from the 4th Federal Interagency Hydrologic Modeling Conference.

Schaake, J.C., Koren, V.I., Duan, Q.-Y., Mitchell, K., Chen, F., 1996. Simple water balance model for estimating runoff at different spatial and temporal scales. Journal of Geophysical Research: Atmospheres 101, 7461–7475. https://doi.org/10.1029/95JD02892

Seo, D.-J., 2012. Conditional bias-penalized kriging (CBPK). Stoch Environ Res Risk Assess 27, 43–58. https://doi.org/10.1007/s00477-012-0567-z

Seo, D.-J., Cajina, L., Corby, R., Howieson, T., 2009. Automatic state updating for operational streamflow forecasting via variational data assimilation. Journal of Hydrology 367, 255–275. https://doi.org/10.1016/j.jhydrol.2009.01.019

Seo, D.-J., Koren, V., Cajina, N., 2003. Real-time variational assimilation of hydrologic and hydrometeorological data into operational hydrologic forecasting. Journal of Hydrometeorology 4, 627–641. https://doi.org/10.1175/1525-7541(2003)004<0627:RVAOHA>2.0.CO;2

Seo, D.-J., Saifuddin, M.M., Lee, H., 2018a. Conditional bias-penalized Kalman filter for improved estimation and prediction of extremes. Stochastic Environmental Research and Risk Assessment 32, 183–201. https://doi.org/10.1007/s00477-017-1442-8

Seo, D.-J., Saifuddin, M.M., Lee, H., 2018b. Correction to: Conditional bias-penalized Kalman filter for improved estimation and prediction of extremes. Stoch Environ Res Risk Assess 32, 3561–3562. https://doi.org/10.1007/s00477-018-1626-x

Seo, D.-J., Seed, A., Delrieu, G., 2010. Radar-based rainfall estimation, in: AGU Book Volume on Rainfall: State of the Science, F. Testik and M. Gebremichael, Editors., Geophysical Monograph Series.

Seo, D.-J., Siddique, R., Zhang, Y., Kim, D., 2014. Improving real-time estimation of heavy-to-extreme precipitation using rain gauge data via conditional bias-penalized optimal estimation. Journal of Hydrology 519, 1824–1835. https://doi.org/10.1016/j.jhydrol.2014.09.055

Shen, H., Lee, H., Seo, D.-J., 2019. Adaptive conditional bias-penalized Kalman filter for improved estimation of extremes and its approximation for reduced computation. arXiv:1908.00482 [eess].

Tang, B., 1993. Orthogonal array-based latin hypercubes. Journal of the American Statistical Association 88, 1392–1397. https://doi.org/10.1080/01621459.1993.10476423

USDA, 1986. Urban hydrology for small watersheds. 2nd edition (Technical Report). U.S. Dept. of Agriculture, Soil Conservation Service, Engineering Division.

van Velzen, N., Altaf, M.U., Verlaan, M., 2016. OpenDA-NEMO framework for ocean data assimilation. Ocean Dynamics 66, 691–702. https://doi.org/10.1007/s10236-016-0945-z

Wickham, J., Stehman, S.V., Neale, A.C., Mehaffey, M., 2020. Accuracy assessment of NLCD 2011 percent impervious cover for selected USA metropolitan areas. International Journal of Applied Earth Observation and Geoinformation 84, 101955. https://doi.org/10.1016/j.jag.2019.101955

World Meteorological Organization, 1992. Simulated real-time intercomparison of hydrological models. Secretariat of the World meteorological organization, Geneva, Switzerland.

Zhang, J., Howard, K., Langston, C., Kaney, B., Qi, Y., Tang, L., Grams, H., Wang, Y., Cocks, S., Martinaitis, S., Arthur, A., Cooper, K., Brogden, J., Kitzmiller, D., 2016. Multi-Radar Multi-Sensor (MRMS) quantitative precipitation estimation: initial operating capabilities. Bulletin of the American Meteorological Society 97, 621–638. https://doi.org/10.1175/BAMS-D-14-00174.1

Zhang, J., Howard, K., Langston, C., Vasiloff, S., Kaney, B., Arthur, A., Van Cooten, S., Kelleher, K., Kitzmiller, D., Ding, F., Seo, D.-J., Wells, E., Dempsey, C., 2011. National Mosaic and Multi-Sensor QPE (NMQ) system: description, results, and future plans. Bulletin of the American Meteorological Society 92, 1321–1338. https://doi.org/10.1175/2011BAMS-D-11-00047.1

Zupanski, D., 2009. Information measures in ensemble data assimilation, in: Park, S.K., Xu, L. (Eds.), Data Assimilation for Atmospheric, Oceanic and Hydrologic Applications. Springer, Berlin, Heidelberg, pp. 85–95. https://doi.org/10.1007/978-3-540-71056-1_4

Zupanski, D., Hou, A.Y., Zhang, S.Q., Zupanski, M., Kummerow, C.D., Cheung, S.H., 2007. Applications of information theory in ensemble data assimilation. Quarterly Journal of the Royal Meteorological Society 133, 1533–1545. https://doi.org/10.1002/qj.123

List of figure captions

Fig 1: a) The 3-basin study area with commercial impervious (purple) and high-density developed (red) areas in the background. b) State-wide view of the study area. c) USGS 24-category and d) NLCD land cover in the study area.

Fig 2: Event total rainfall maps (in mm) for the a) Jan 2017, b) Feb 2018, c) Sep 2018 and d) May 2019 events.

Fig 3: Simulation results from event-specific (black) and non-event-specific (red) calibration vs. the observed (blue empty circles) for the a) JC Jan 2017, b) CC Jan 2017, c) FC Feb 2018 and d) JC Sep 2018 cases.

Fig 4: a) Multiplicative factors to Manning's n for channel routing obtained from event-specific calibration. b) Non-event-specific estimates of Manning's n for channel routing obtained from averaging for each catchment the middle 3 of the 5 values in a).

Fig 5: a) Comparison of simulated peak flow from event-specific (black) and non-event-specific (red) calibration vs. the observed for all 15 cases except for the JC Feb 2018 case. The symbols "J", "C" and "F" denote the JC, CC and FC results, respectively. The solid, dashed and dotted gray lines represent ± 10, 20 and 30% errors. b) Same as a) but for time-to-peak flow. The solid, dashed and dotted gray lines represent ± 1, 2 and 3-hr errors.

Fig 6: Comparison of simulated hydrographs forced by 1-min (black) and 1-min average of 10-min (red) CASA QPE vs. the observed (blue empty circles) for the JC May 2019 case.

Fig 7: Same as Fig 5 but the comparison is among the 250 m LSM and 250 m routing (black), 250 m LSM and 125 m routing (red) and 250 m LSM and 50 m routing (green) results.

Fig 8: Histograms of stream order as modeled at resolutions of a) 125 m and b) 50 m.

Fig 9: Same as Fig 5a but the comparison is for a) the NLCD (black) vs. the USGS 24-category (red) land cover results, and b) the CASA QPE (black) vs. the NLDAS QPE (red) results.

Fig 10: DA-aided ensemble predictions (cyan), ensemble mean prediction (blue) and DA-unaided base predictions based on non-event-specific calibration (red) vs. the observed (blue empty circles) for the a) FC Jan 2017, b) CC Feb 2018, c) FC Feb 2018 and d) CC Sep 2018 cases. The green and black lines show the ensemble DA analysis within the assimilation window and the prediction time, respectively.

Fig 1

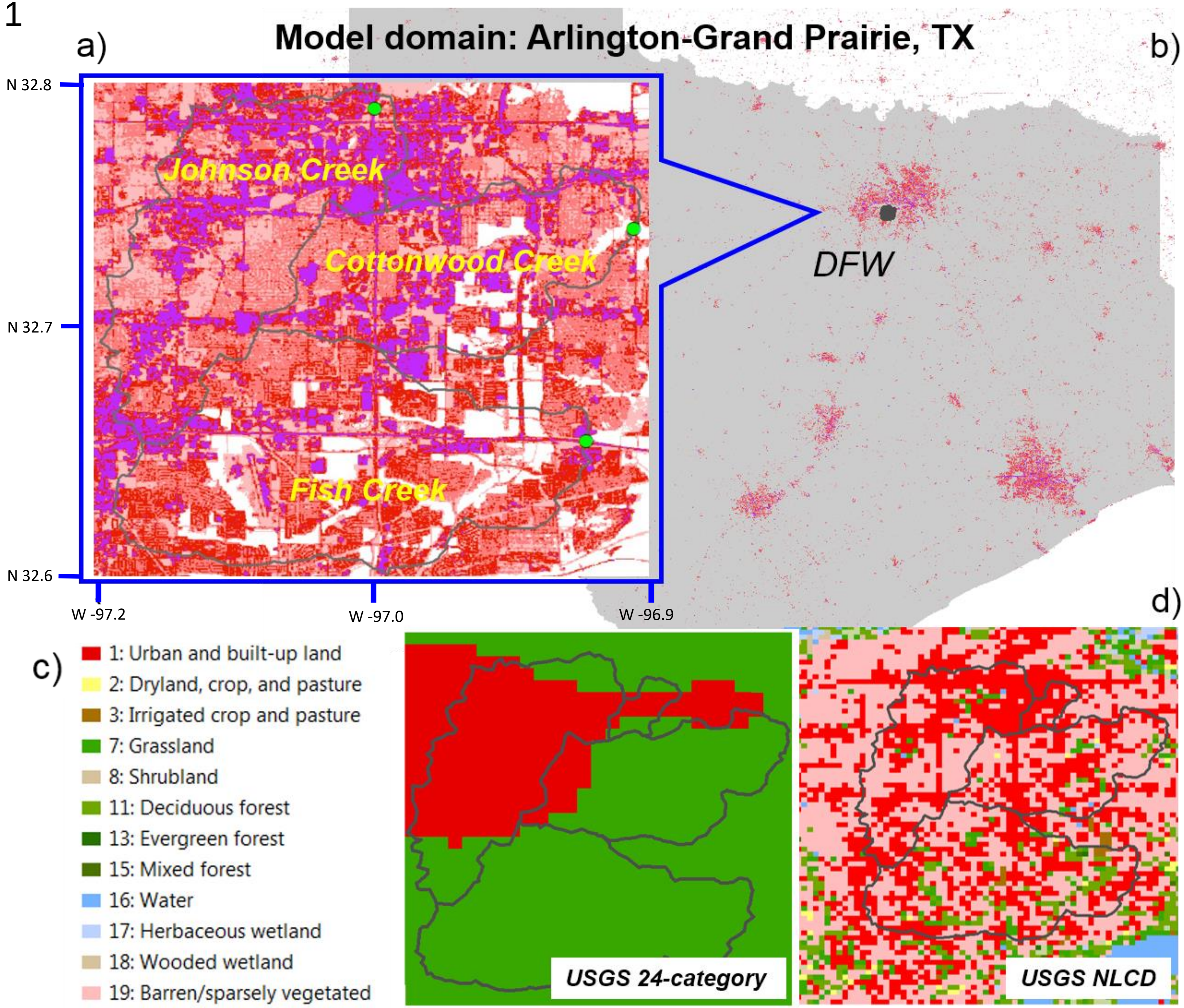

a)
Model domain: Arlington-Grand Prairie, TX
b)
N 32.8
N 32.7
N 32.6
W -97.2
W -97.0
W -96.9
Johnson Creek
Cottonwood Creek
Fish Creek
DFW
c)
1: Urban and built-up land
2: Dryland, crop, and pasture
3: Irrigated crop and pasture
7: Grassland
8: Shrubland
11: Deciduous forest
13: Evergreen forest
15: Mixed forest
16: Water
17: Herbaceous wetland
18: Wooded wetland
19: Barren/sparsely vegetated
d)
USGS 24-category
USGS NLCD

Fig 2

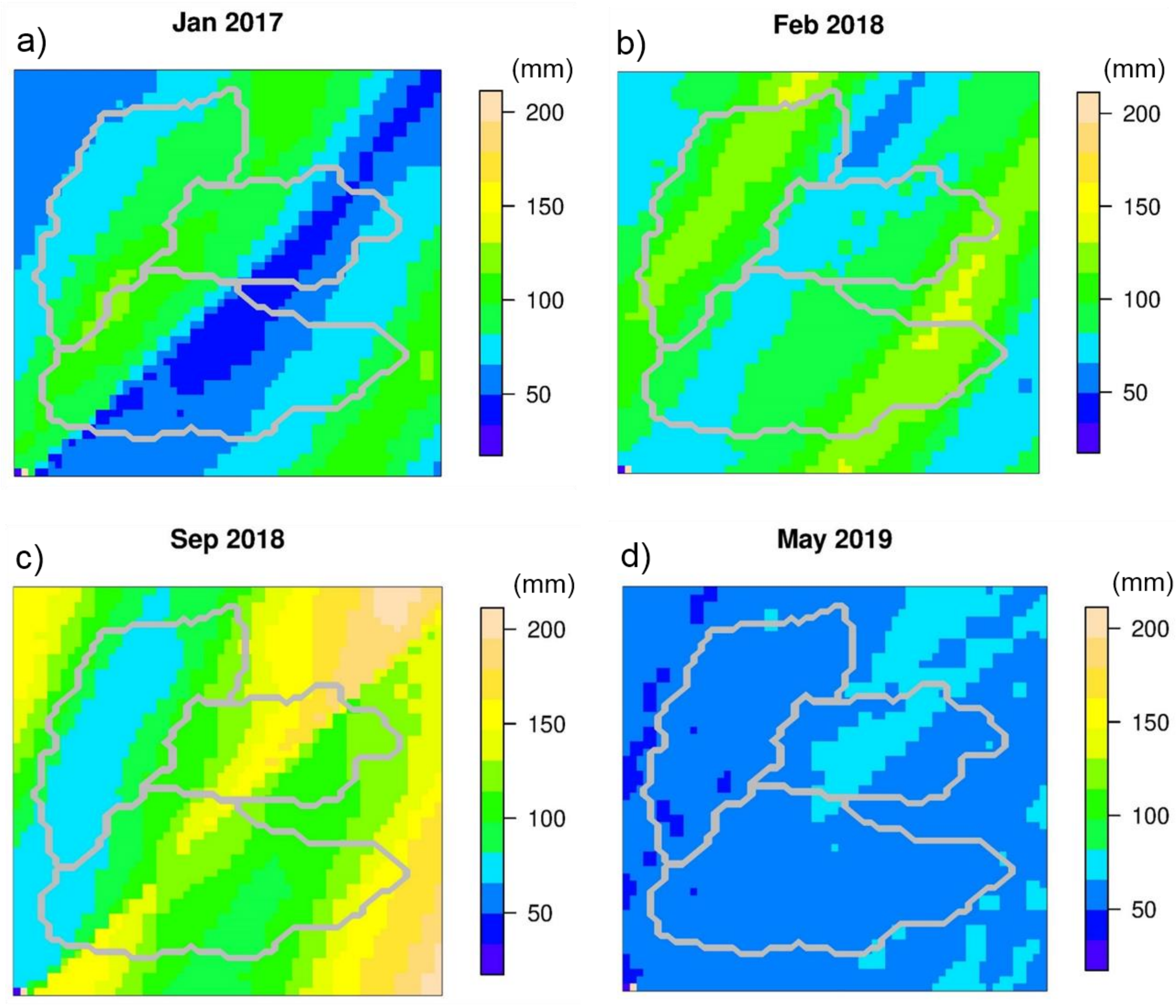
a)
Jan 2017
(mm)
200
150
100
50
b)
Feb 2018
(mm)
200
150
100
50
c)
Sep 2018
(mm)
200
150
100
50
d)
May 2019
(mm)
200
150
100
50

Fig 3

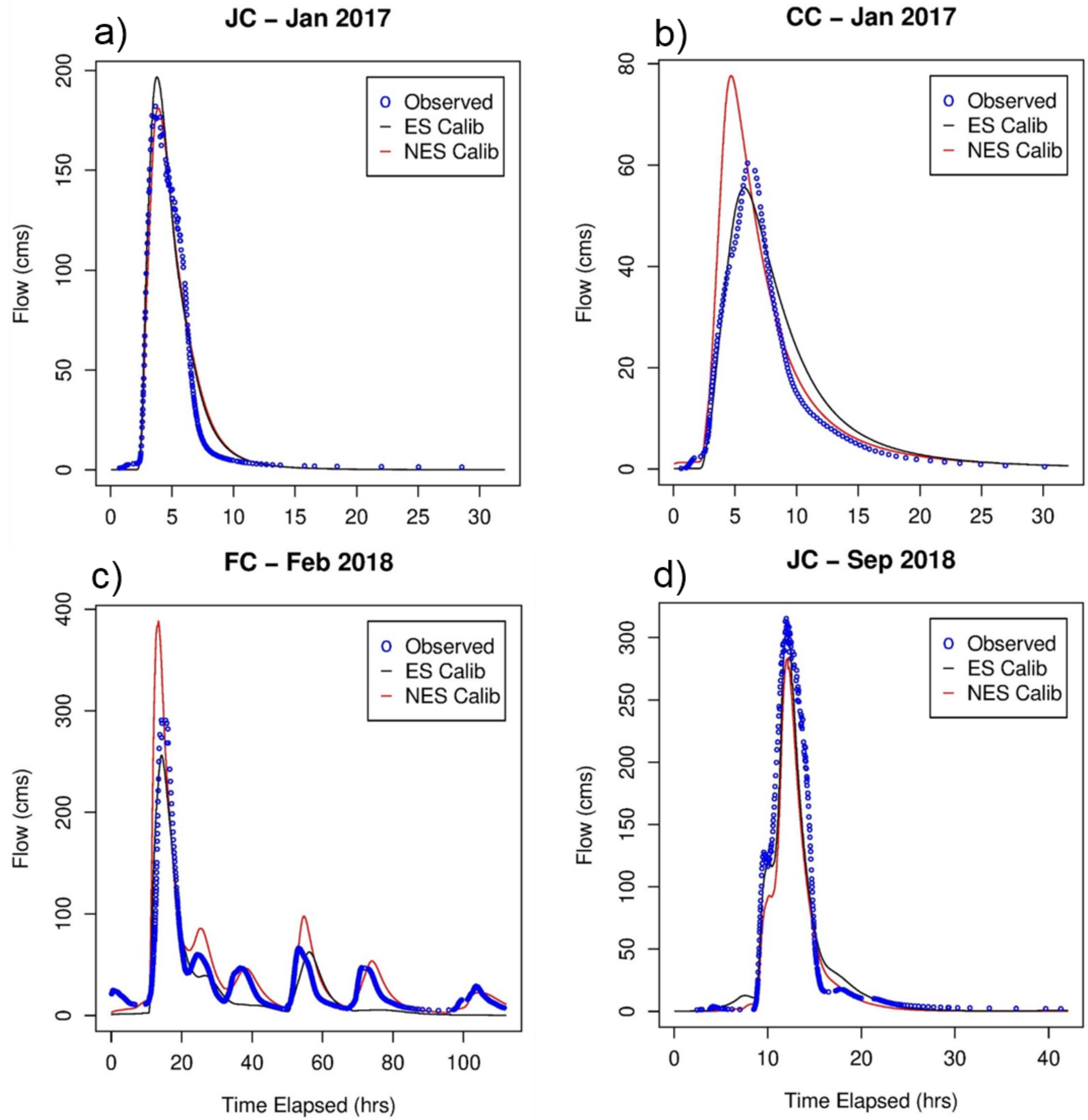
a)
JC – Jan 2017
Observed
ES Calib
NES Calib
Flow (cms)
b)
CC – Jan 2017
Observed
ES Calib
NES Calib
Flow (cms)
c)
FC – Feb 2018
Observed
ES Calib
NES Calib
Flow (cms)
Time Elapsed (hrs)
d)
JC – Sep 2018
Observed
ES Calib
NES Calib
Flow (cms)
Time Elapsed (hrs)

Fig 4

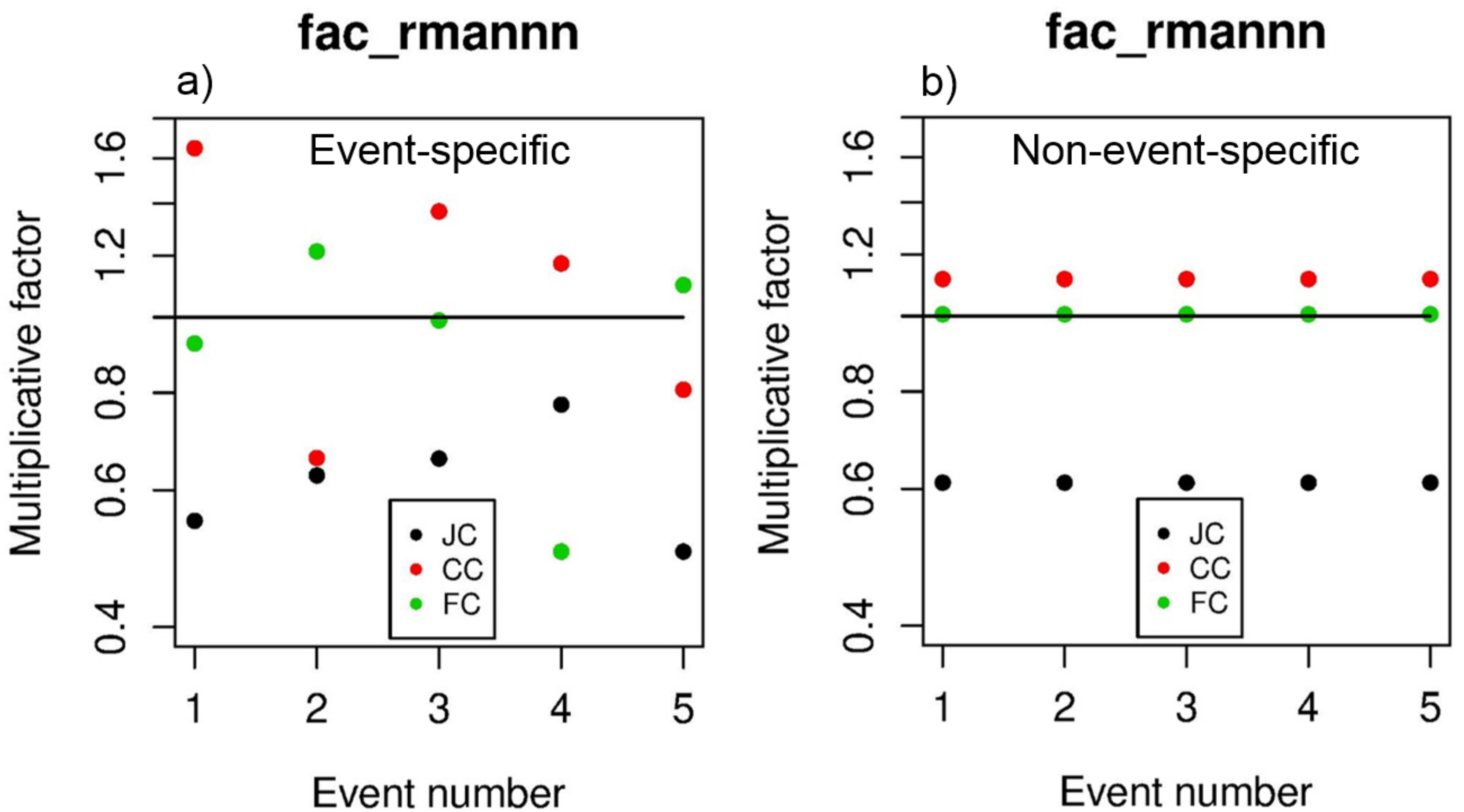
fac_rmannn
a)
Event-specific
Multiplicative factor
0.4
0.6
0.8
1.2
1.6
JC
CC
FC
1
2
3
4
5
Event number
fac_rmannn
b)
Non-event-specific
Multiplicative factor
0.4
0.6
0.8
1.2
1.6
JC
CC
FC
1
2
3
4
5
Event number

Fig 5

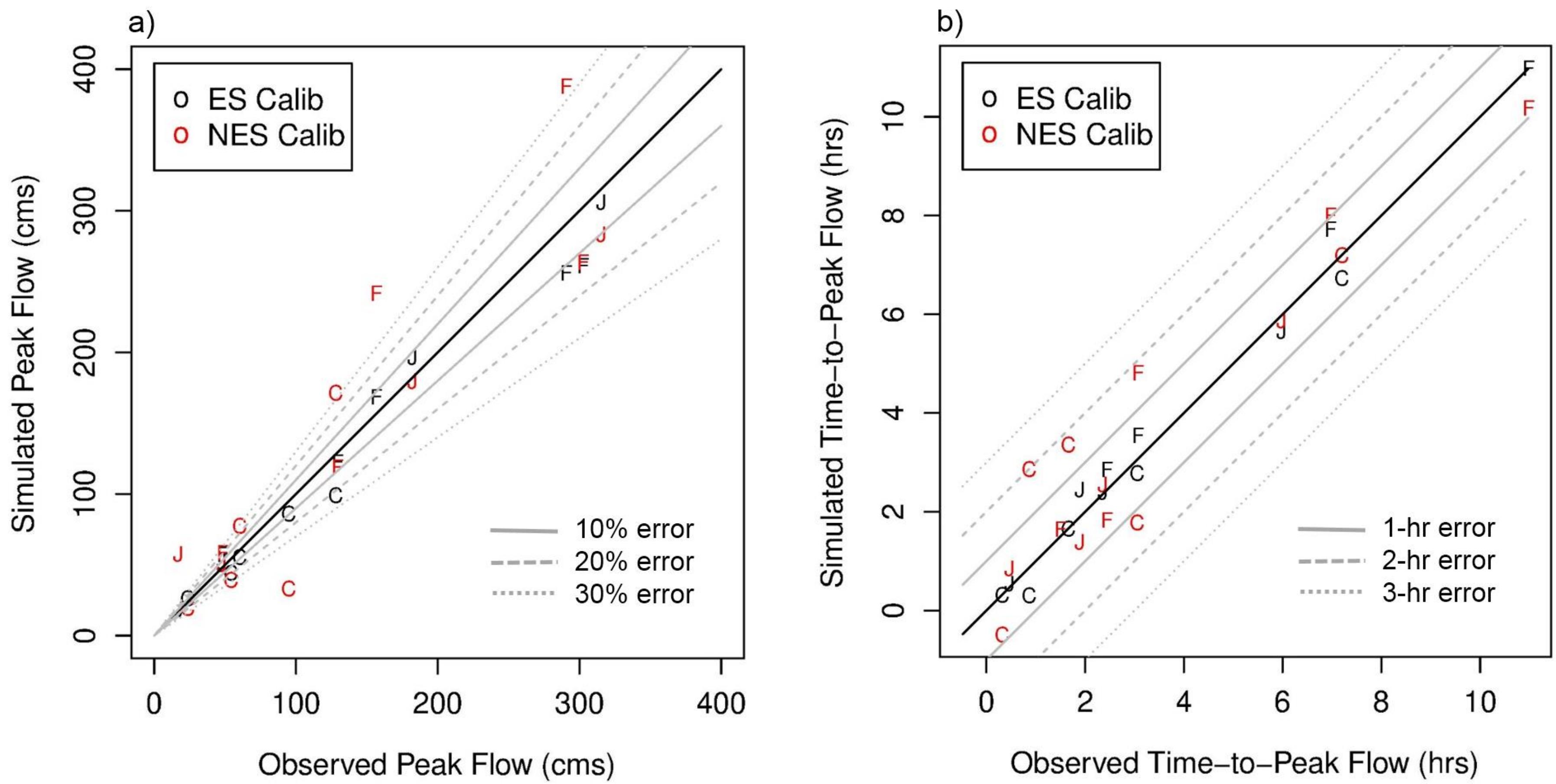
a)
o ES Calib
o NES Calib
10% error
20% error
30% error
Simulated Peak Flow (cms)
Observed Peak Flow (cms)
0
100
200
300
400
b)
o ES Calib
o NES Calib
1-hr error
2-hr error
3-hr error
Simulated Time−to−Peak Flow (hrs)
Observed Time−to−Peak Flow (hrs)
0
2
4
6
8
10

Fig 6

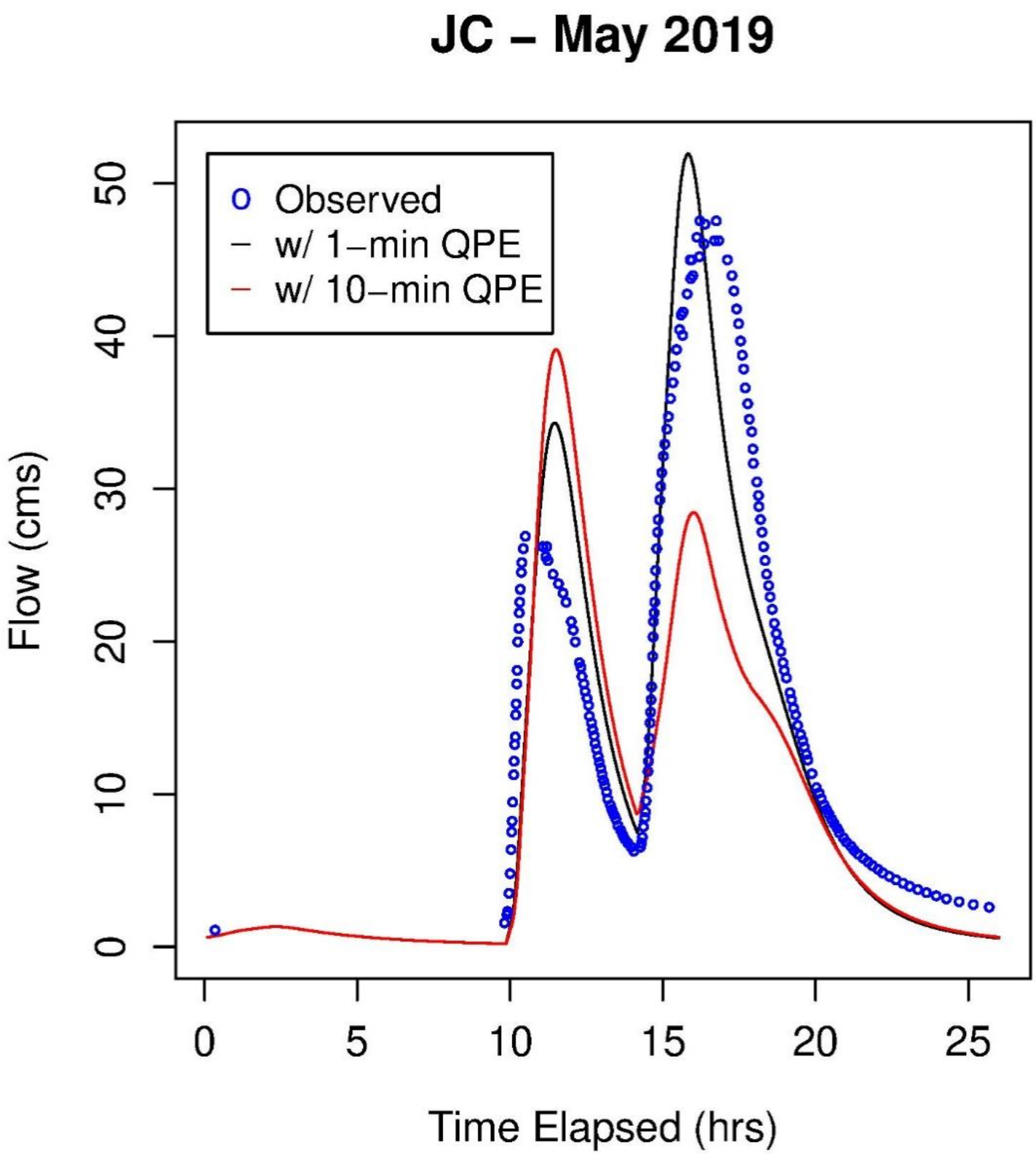

JC – May 2019
Observed
w/ 1–min QPE
w/ 10–min QPE
Flow (cms)
0
10
20
30
40
50
0
5
10
15
20
25
Time Elapsed (hrs)

Fig 7

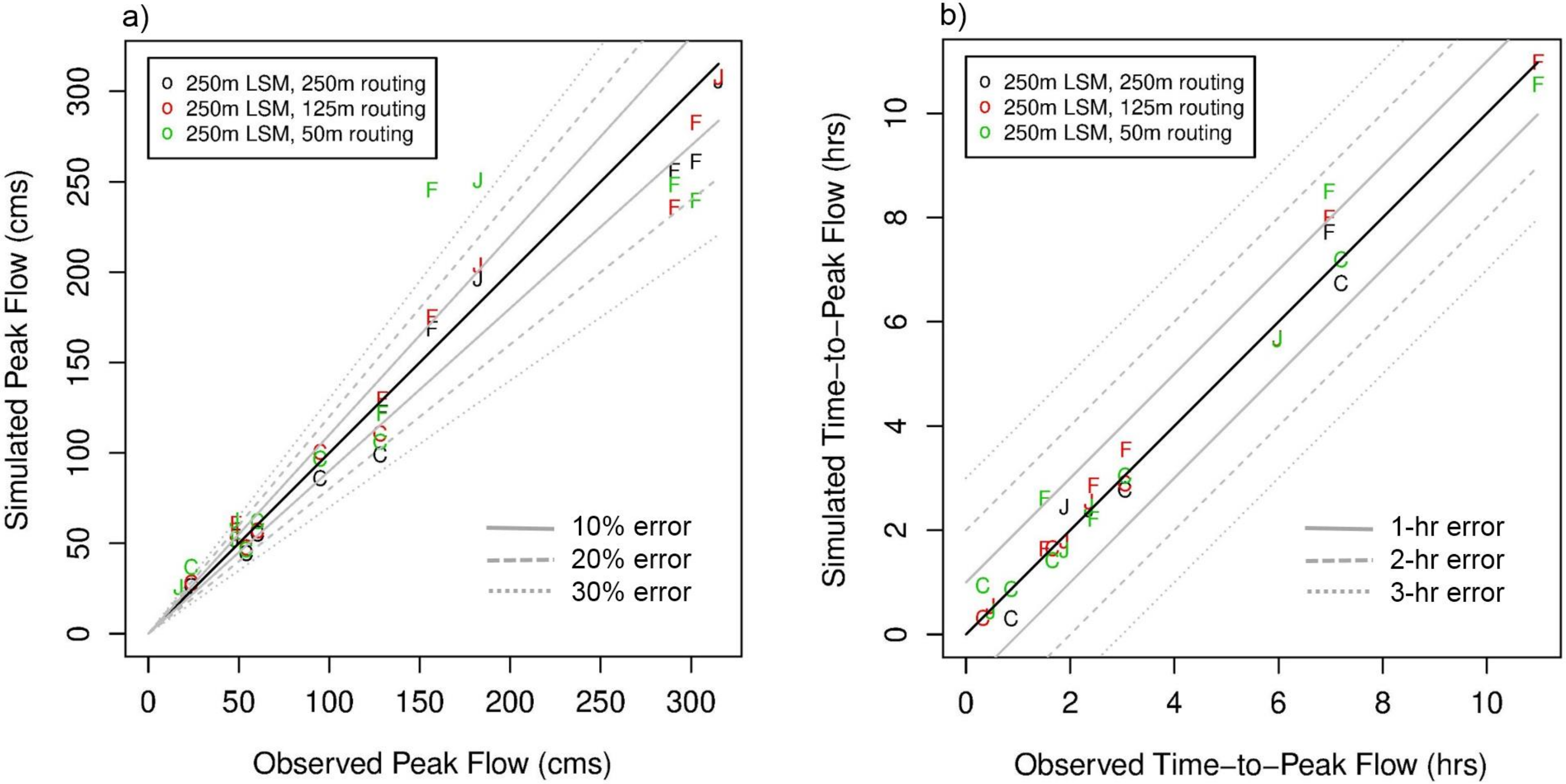

a)
o 250m LSM, 250m routing
o 250m LSM, 125m routing
o 250m LSM, 50m routing
10% error
20% error
30% error
Simulated Peak Flow (cms)
Observed Peak Flow (cms)
b)
o 250m LSM, 250m routing
o 250m LSM, 125m routing
o 250m LSM, 50m routing
1-hr error
2-hr error
3-hr error
Simulated Time−to−Peak Flow (hrs)
Observed Time−to−Peak Flow (hrs)

Fig 8

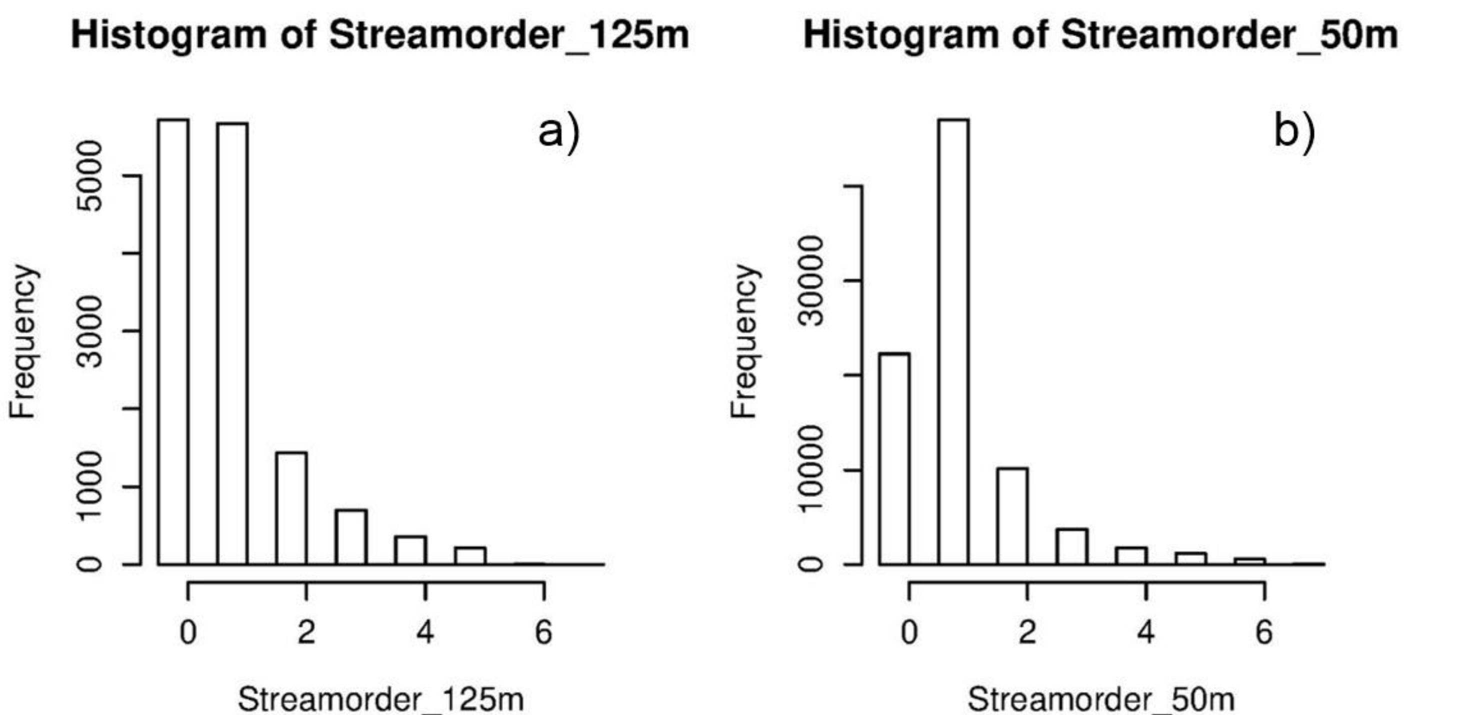
Histogram of Streamorder_125m
a)
Frequency
0
1000
3000
5000
0
2
4
6
Streamorder_125m
Histogram of Streamorder_50m
b)
Frequency
0
10000
30000
0
2
4
6
Streamorder_50m

Fig 9

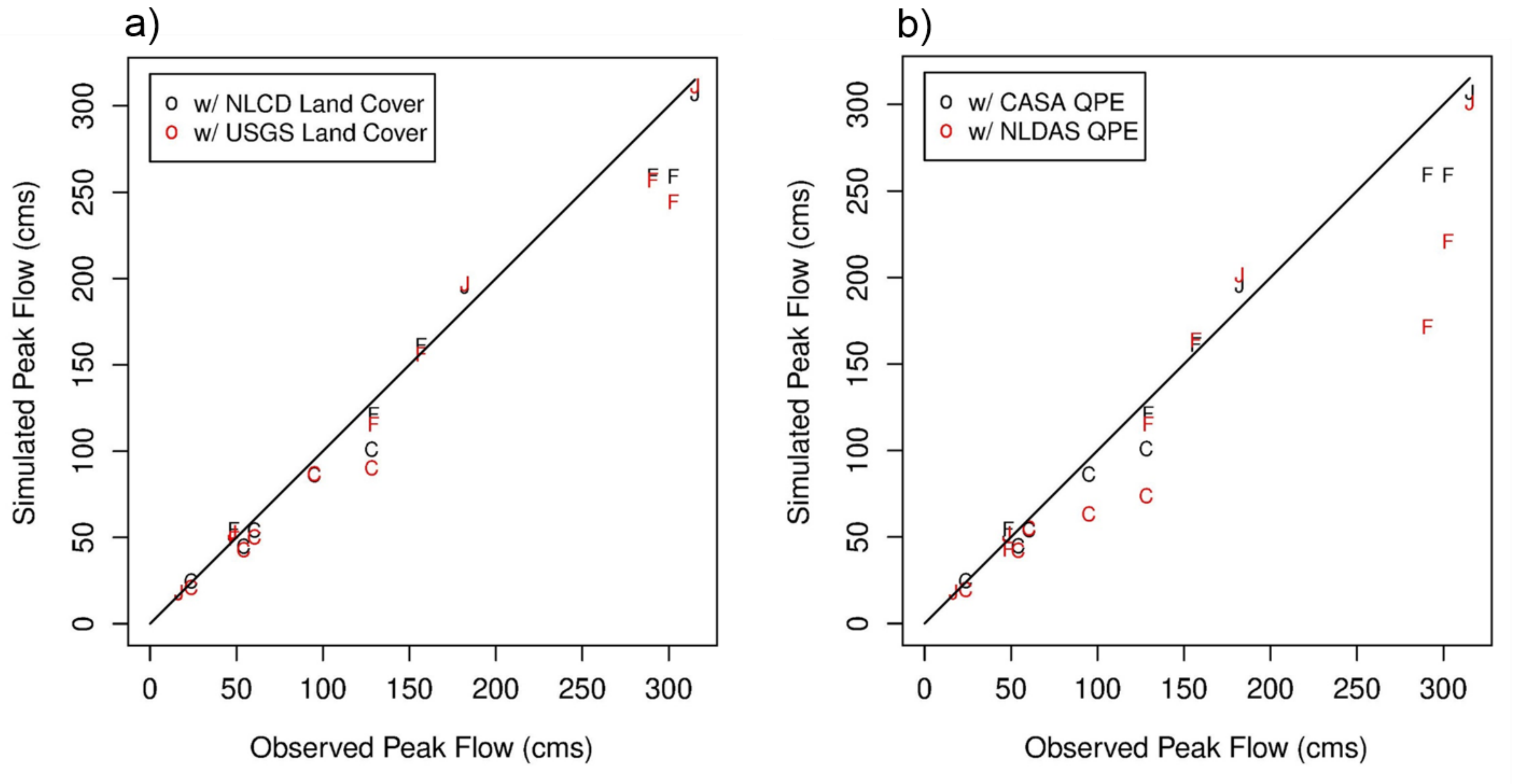
a)
o w/ NLCD Land Cover
o w/ USGS Land Cover
Simulated Peak Flow (cms)
Observed Peak Flow (cms)
0
50
100
150
200
250
300
b)
o w/ CASA QPE
o w/ NLDAS QPE
Simulated Peak Flow (cms)
Observed Peak Flow (cms)
0
50
100
150
200
250
300

Fig 10

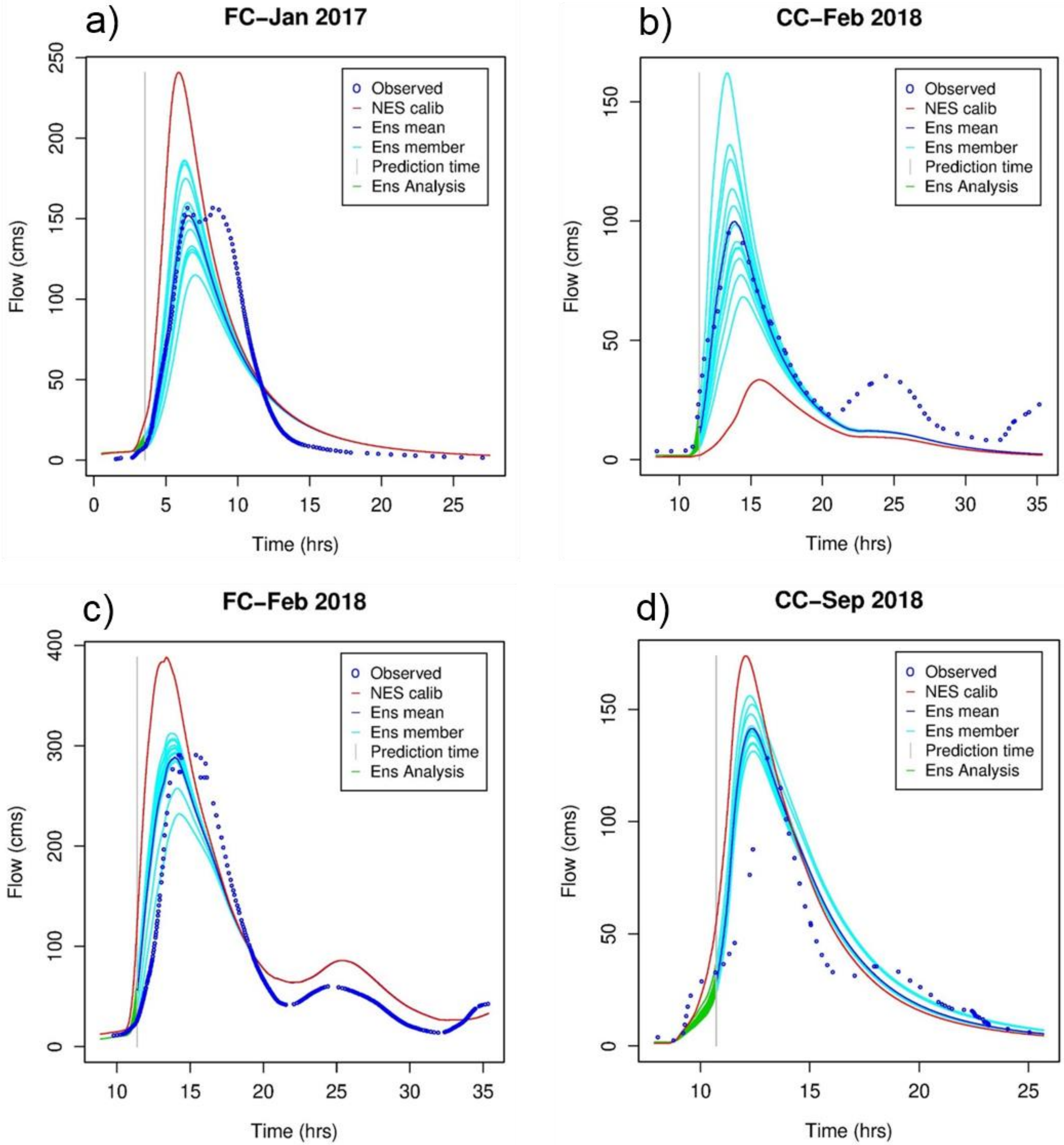

a)
FC–Jan 2017
b)
CC–Feb 2018
c)
FC–Feb 2018
d)
CC–Sep 2018
Observed
NES calib
Ens mean
Ens member
Prediction time
Ens Analysis
Flow (cms)
Time (hrs)

Table 1. List of rainfall events used.

Event	Event total mean areal rainfall (mm)			Period of record	Duration
	JC[1]	CC[2]	FC[3]		
Jan 2017	75.8	90.8	71.6	00:00Z 01/16/2017 - 23:59Z 01/17/2017	48 hrs
Feb 2018	95.2	93.7	100.5	00:00Z 02/20/2018 - 07:59Z 02/21/2018	32 hrs
Sep 2018	97.6	103.1	131.9	12:00Z 09/21/2018 - 19:59Z 09/22/2018	32 hrs
Apr 2019	31.5	33.5	27.1	00:00Z 04/17/2019 – 11:28Z 04/18/2018	35 hrs
May 2019	56.5	60.1	62.5	00:00Z 05/08/2019 – 03:43Z 05/09/2019	28 hrs

[1]Johnson Creek Catchment
[2]Cottonwood Creek Catchment
[3]Fish Creek Catchment

Table 2. Combinations of spatio-temporal resolutions used.

	QPE	Rainfall-runoff	Terrain and channel routing
Spatial	125, 250, 500 m (all at 1 min resolution)	125, 250 m	50, 125, 250 m
Temporal	1, 10 min (both at 250 m resolution)	1 min timestep	15 sec timestep

Table 3. Wall clock times (in sec) for a 32-hr WRF-Hydro simulation[1]

Resolution (m)		Number of threads			
LSM	Routing models	4	8	16	32
250	250	32	18	13	11
250	125	63	37	26	22
250	50	1043	637	386	264
125	125	150	79	48	43

[1] On Intel(R) Xeon(R) Gold 6152 CPU @ 2.10GHz 44 CPU core (2 threads/core) Linux computer